Emily Black ORCID: https://orcid.org/0000-0003-1344-6186

Contrasting rainfall and heat risks to southern African maize during El Niño

Emily Black[a,b] and Philip Frost[c]

[a] *Department of Meteorology, University of Reading, Reading, UK*

[b] *National Centre for Atmospheric Science (NCAS), Reading, UK*

[c] *TomorrowNow.org, 9 Channel Center Street, Seventh Floor, Boston, MA 02210*

Corresponding author: Emily Black
e.c.l.black@reading.ac.uk

Preprint for EarthArXiv

This manuscript has not been peer reviewed.

Submitted to *Environmental Research Communications*.

11 November 2026

The main paper is followed by the complete Supplementary Information.

© 2026 The authors. This preprint is licensed under a Creative Commons Attribution 4.0 International licence (CC BY 4.0): https://creativecommons.org/licenses/by/4.0/.

Abstract

El Niño poses substantial risks to maize production in southern Africa, but the relative contributions of rainfall deficits and heat, and the opportunities to anticipate these hazards, vary geographically. We combine historical climate–yield analysis across ten southern African countries with verification of forecasts from two models to assess these risks and their predictability. National and sub-national maize yield records and gridded climate data are used to characterise climate–yield relationships and statistically decompose El Niño-associated yield differences into rainfall and heat contributions. These analyses reveal that the estimated rainfall contribution is larger in Zimbabwe and Mozambique, whereas the estimated heat contribution is larger in South Africa, Namibia and Zambia. For both temperature and rainfall, forecast skill is generally greatest for the first month after initialisation. At longer leads, rainfall skill approaches climatological levels in most regions, while temperature and compound dry–hot forecasts retain skill in some areas. In the northern part of the domain, rainfall forecast skill for March at one-month lead improves during El Niño, suggesting enhanced opportunities for early warning. Overall, the findings of this study demonstrate the importance of matching agricultural early warning to regional differences in climate–yield sensitivity and forecast skill. In particular, temperature forecasts offer opportunities to anticipate agricultural hazards where heat contributes substantially to yield reductions, even when rainfall forecast skill is limited.

1 Introduction

Farmers in the Global South depend on staple food crops, such as maize, for both income and subsistence [1]. In much of southern Africa, a hot, seasonally dry climate and limited access to irrigation render crops vulnerable to adverse weather [2]. The widespread and severe drought conditions associated with El Niño [3-6] thus pose substantial risk to crop yields [7-12] and hence to livelihoods [13, 14]. Understanding this threat is a key priority for humanitarian, governmental and non-governmental organisations – especially during the build-up to strong El Niño events [15, 16].

Climate-related risks to agriculture depend on the sensitivity of crops to variations in temperature and rainfall. Both high and low rainfall can be hazardous, with high rainfall causing water-logging and increased disease burden, and low rainfall causing water stress and poor growth [17, 18]. Very high and low temperatures are also detrimental to crops, with cold conditions slowing photosynthesis and limiting growth, and heat stress causing irreversible cellular damage [17, 19]. The effect of an El Niño event on crop yield at a given location thus depends on both the magnitude of temperature and precipitation anomalies and the underlying climate on which the anomalies are imposed (Figure S1).

Previous studies have identified geographically varying links between ENSO and crop yields [20]. In southern and East Africa, an observational study found associations between maize yield and ENSO-related rainfall and soil-moisture anomalies, although with variation between countries and individual events [21]. Another study used climate-model simulations and observations to assess the impact of high temperatures and low rainfall on maize production in South Africa, highlighting the potential risk to yield due to unprecedented high temperatures during strong El Niño events [22]. Comparison between these analyses highlights the complexity of the interactions between local climate, crop sensitivity and ENSO

teleconnections. The relative importance of rainfall and heat for yield risk therefore cannot be assumed to be uniform across southern Africa, particularly during strong El Niño events.

Early warning of adverse meteorological conditions is of great value to governments and humanitarian organisations – especially when anomalies are expected to be large and widespread. Although the broad effects of El Niño are well understood [3], the regional patterns of anomalies vary considerably from one event to another [23, 24]. For example, the widespread southern African drought anticipated during the strong 1997/98 El Niño failed to materialise in the northern parts of southern Africa, whereas the 2015/16 event brought exceptionally dry conditions across the region [25, 26]. Thus, whilst assessments of historical El Niño events have value, meteorological forecasts play a key part in identifying regions at severe risk during individual events. This is especially the case because the anticipation of an El Niño can affect farmer decision-making, behaviour and food markets [27]. Although the skill of precipitation forecasts declines markedly beyond ~3 weeks [28], temperature forecasts retain skill over longer lead times [29]. Moreover, the presence of an El Niño may itself enhance or reduce skill [29, 30].

The utility of meteorological forecasts for anticipatory action hinges on their skill for forecasting impact relevant metrics at leads of relevance for decision-making and planning [31]. For regions where yield variability is affected by temperature, skilful forecasts of very hot conditions several weeks in advance may provide useful information – even when precipitation forecasts are highly uncertain. Looking to the future, a new generation of machine-learning forecasting models [32, 33] may improve precipitation and temperature forecast skill at longer leads, especially for regions such as Africa, where precipitation anomalies are potentially predictable on seasonal time scales [34, 35].

This paper investigates climate-related risks to agriculture during El Niño events. We focus on southern Africa because of the significantly increased risk of drought during El Niño [3, 36], and on maize because of its importance for regional food security and its sensitivity to drought [37]. Specifically, we address the following questions:

- What are the relative contributions of rainfall and temperature anomalies to yield risk during El Niño across southern Africa?
- How skilfully can these meteorological conditions be predicted up to two months ahead, and how does forecast skill differ between El Niño and non-El Niño years?

Our approach combines analysis of rainfall and temperature contributions to El Niño-related yield anomalies with meteorological forecast evaluation. A systematic comparison across ten southern African countries enables us to investigate regional differences in the climatic pathways of yield risk. This provides a basis for assessing where rainfall and temperature forecasts offer opportunities to anticipate agricultural hazards.

2 Data and Methods

2.1 Data

2.1.1 Observational data

The primary national maize-yield data were obtained from the Food and Agriculture

Organization (FAO) (http://faostat.fao.org/) to provide consistent country-level coverage across the study region. Supplementary sub-national analyses were conducted using the HarvestStat dataset [38]. Maize planting coverage was obtained from the AHAD dataset [39]. For precipitation, the primary dataset used was TAMSAT v3.1 [40-42], supplemented with CHIRPS v3 [43], IMERG Final V07B [44], ERA5 [45] and CPC [46, 47] (see comparisons in Figures S4 and S5). TAMSAT was chosen for the main analyses because previous studies have found it to perform particularly well for diagnosis of dry spells and variability during dry years[40]. TAMSAT's historical calibration, furthermore, suits it for analyses of variability over multiple decades [48, 49]. The primary maximum daily temperature dataset used was the CPC Unified Global Temperature (obtained from https://psl.noaa.gov), supplemented with the ERA5 reanalysis [45]. CPC gridded maximum temperature data were selected for the primary analysis because they provide an observation-based estimate derived from surface-station observations [50]. Further details of the datasets used in the study are included in Supplementary Information (Table S1).

2.1.2 Seasonal hindcasts

Outputs were obtained from two seasonal forecasting systems: the European Centre for Medium Range Weather Forecasting Integrated Forecasting System (ECMWF-IFS) and Google's recently developed NeuralGCM. ECMWF forecasts were obtained from the Copernicus Climate Change Service Climate Data Store, using the SEAS5.1 product on a 1° × 1° grid. The underlying SEAS5 system couples the Integrated Forecasting System atmospheric model to ocean and sea-ice models [51]. Forecast ensembles are initialised on the first day of each month and extend seven months ahead. This study used forecasts covering November and March verification periods, with initialisations on 1 October and 1 November for November, and 1 February and 1 March for March. The evaluated target periods fall within the first two forecast months.

NeuralGCM is a hybrid machine-learning/physics based global atmospheric model that combines learned components with a differentiable dynamical core [32]. Unlike the coupled ECMWF seasonal forecasting system, NeuralGCM does not include an interactive ocean model. SST boundary conditions for the hindcasts used in this study were prescribed by persisting the observed SST anomalies at initialisation. This study uses the precipitation-optimised NeuralGCM configuration, which was trained against satellite-derived precipitation observations [33]. Although higher-resolution NeuralGCM configurations are available for the general weather and climate model, the precipitation-optimised checkpoint is currently available only at approximately 2.8° horizontal resolution (https://neuralgcm.readthedocs.io/en/latest/checkpoints.html). The precipitation-optimised system was selected because the purpose of this study is specifically to assess the predictability of rainfall and rainfall-derived agricultural risks. To maximise the length of the independent validation record, 5-member ensembles of NeuralGCM hindcasts were generated using the publicly available model checkpoint for 1983-1999 and 2021-2025. Forecasts for 2000–2020 are excluded from formal skill assessment (including the comparisons with the ECMWF forecasts) because this period overlaps the training period of the precipitation model and therefore cannot be regarded as an independent evaluation sample.

2.1.3 Data processing

All gridded observational and hindcast data were placed on the common 0.25° TAMSAT grid. TAMSAT was obtained as the provider's 0.25° product. To avoid penalising NeuralGCM for its low resolution, for the NeuralGCM and ECMWF comparisons shown in Figure 5 and Figure S23, the hindcast data were downscaled using a simple analogue method (see Supplementary Information). For the ECMWF skill assessments shown in Figure 4 and Figure 6, the analogue downscaling method was not used, and the data were re-gridded to the common 0.25° grid using bilinear interpolation.

2.2 Methods

2.2.1 Masking on local growing seasons and maize cultivation regions

This study focuses on maize cultivation for ten countries in southern Africa (see Figure 1 for the domain). To provide a fair comparison between climate and yield, the climate–yield analyses in Sections 3.1 and 3.2 use climate exposure within the assumed growing season and maize-growing areas. For these analyses, meteorological data are masked spatially on the AHAD maize coverage map [39] (Figure S2), and temporally on local growing seasons (Figure S3). Forecast maps in Section 3.3 cover the full analysis domain and use fixed November and March target periods; maize-area summaries are identified separately.

Local growing seasons are approximated by the diagnosed rainy seasons. This limits the counting of heat and dry-spell exposure outside the period when crops are assumed to be growing. The seasonal timing is diagnosed at each grid cell using a well-established objective method in which onset and cessation are determined separately for each season year [52, 53]. Climate metrics are then calculated within these spatially and temporally varying season windows rather than over fixed calendar months. Where annual timing is unusable, the corresponding local climatological season is used for rainfall and heat exposure. Country-level values are calculated over maize-growing grid cells using cosine-latitude area weights. Further details of the methodologies by which the maize and rainy season masks are created are given in the Supplementary Information.

2.2.2 Comparison between variability in maize yield and climate

FAOSTAT harvest year Y is aligned with the rainy season beginning in the preceding calendar year (season_year = Y − 1); for example, the 2024 harvest is paired with the 2023/24 season. The country-level climate–yield analysis covers 1983/84–2023/24. Forty seasons have complete rainfall, temperature and yield data; 1984/85 is excluded because the CPC temperature record does not meet the coverage requirement.

The aim of this study is to assess climatic risk to yield during El Niño events – in particular how rainfall and heat anomalies contribute to anomalously low or high values. Over the long term, global yield (and regional yield at some localities) has steadily increased as a result of improved technology, intensification of agricultural practices and better access to farm inputs [54, 55]. In order to assess performance against contemporary production conditions rather than a long term historical baseline, interannual variability in maize yield is represented using a local five-harvest rank, with each season ranked from 1 (lowest) to 5 (highest) among the five closest available harvests. As well as suppressing the agricultural technology trend, local comparison may also suppress gradual climate-driven changes in yield – enabling us to focus on event-related anomalies rather than long term trends. The use of a local yield baseline

follows the rationale of Iizumi et al. [20], who calculated anomalies relative to a five-year running mean. The use in our study of ranking rather than absolute anomalies emphasises relative harvest performance rather than the magnitude of yield anomalies. Ranking the data in this way reduces the effect of outliers and provides a common scale for comparison across countries and regions. The sensitivity of the results to using a ranking rather than a percentage anomaly is illustrated in Figure S11.

Climate exposure is represented primarily using three metrics calculated over each grid cell's locally diagnosed rainy season: total seasonal rainfall; the number of days with maximum temperature above 32°C; and the number of compound dry–hot days, defined as days with maximum temperature above 32°C that immediately follow at least five consecutive days with rainfall below 1 mm. For forecast verification, we also evaluate 30-day accumulated rainfall, 30-day mean maximum temperature and 30-day compound dry–hot-day counts over the target periods. Definitions of all primary and supplementary metrics used in the study are given in Table S2.

2.2.3 Investigation of rainfall and temperature contributions during El Niño events

For the El Niño analysis, seasons are classified as moderate, strong or very strong El Niño using the NOAA Oceanic Niño Index (ONI), with all other seasons forming the non-El Niño reference group. The seasons included and the evolution of the ONI from July of year zero to June of year one are shown in Figure S12. To decompose the El Niño-associated yield difference at country level, we fit multiple linear regressions of maize-yield rank on standardised seasonal rainfall and rainy-season hot-day counts, using all available complete seasons. The predictors are fitted jointly, so each coefficient describes its association with yield rank after accounting for the other predictor. Figure 1 presents these fitted climate–yield sensitivities, including a separate model in which compound dry–hot-day counts replace hot-day counts. Figure 3 combines the rainfall and hot-day sensitivities with the corresponding El Niño climate differences to estimate their contributions to the observed yield difference. Predictors are standardised using each country's 1991–2020 mean and standard deviation, and contributions are calculated by multiplying the fitted coefficients by the corresponding El Niño-minus-non-El Niño climate differences.

We use a parsimonious additive model to estimate separate rainfall and heat contributions, with a rainfall–heat interaction assessed as an exploratory sensitivity check (Table S3). Joint modelling of rainfall and temperature was previously applied to South African maize by Bradshaw et al. [22], who also omitted an interaction term, although their model retained quadratic responses. Our regression provides a statistical decomposition rather than a causal attribution.

Uncertainty in climate–yield coefficients and El Niño decomposition terms is assessed using 2,000 bootstrap resamples of complete season values. For each country or administrative unit, the paired climate and yield observations from complete seasons are resampled with replacement, and the corresponding regression is then refitted for each bootstrap sample. For the El Niño decomposition, El Niño and non-El Niño seasons are resampled separately, with the regression coefficients and the differences between El Niño and other season climate recalculated for each iteration. The 2.5th and 97.5th percentiles of the bootstrap distributions define pointwise 95% uncertainty intervals. A relationship or contribution is considered robust

when its interval excludes zero. Further details, including diagnostics of predictor dependence and sensitivity to omitting individual El Niño seasons and episodes, are given in the Supplementary Information.

2.2.4 Forecast skill assessment

Forecast skill is assessed using the receiver operating characteristic area under the curve (ROC-AUC) and the Pearson anomaly correlation coefficient (ACC, or *r*). ACC is calculated from anomalies relative to the relevant climatological reference. ROC-AUC assesses discrimination of lower-tercile rainfall events and upper-tercile temperature metrics, with tercile thresholds calculated separately for each observed grid cell over the verification period. ROC-AUC measures event discrimination rather than probability calibration. It should be noted that neither the observations nor the hindcasts are detrended, so the reported skill reflects the models' representation of long-term changes in climate as well as interannual variability. Retaining these changes is relevant to assessing agricultural hazards, particularly heat exposure against a warming background climate. Further details of the forecast pairing, lead-time definitions and verification procedures are provided in the Supplementary Information.

3 Results and Discussion

3.1 Climate-yield relationships across southern Africa

In southern Africa, low yield is generally associated with low rainfall, as well as with greater occurrence of very hot days (>32°C) and compound dry–hot days (Figure 1, Figure S10, Figure S11). These relationships, however, vary regionally. The association with seasonal rainfall is clearest in eastern regions, particularly Mozambique and Zimbabwe, with western regions (Angola and Namibia) exhibiting weaker associations. For the temperature metrics, in contrast, the strongest associations are in the south and west. An exception to this pattern is Angola, where higher temperatures and low rainfall are associated with higher yield, although not at a statistically significant level. In several countries, compound dry–hot-day occurrence has a stronger estimated association with yield than either seasonal rainfall or occurrence of hot days. This is consistent with experimental evidence on the hazard to crop health posed by simultaneously dry and hot conditions [37].

Regional variability in yield–climate relationships is also evident within countries (Figure S9). In South Africa, for example, there is a statistically significant positive association between yield and seasonal precipitation in the northeast, but weak or negative association in the south. Similarly, in Zambia and Mozambique, yield is positively associated with rainfall in the dry south, with weaker/negative associations in wetter northeast regions. Aggregating these opposing regional signals may weaken the relationships apparent in the national data.

Although robust climate-yield associations are evident in several countries, substantial year-to-year variability remains unexplained by the variables analysed (Figure S7). Potential contributors include factors such as agricultural management, pests and diseases [1], and climatic variability not represented by the metrics considered, such as the timing of dry spells [8]. The supplementary analysis supports the relevance of additional metrics of climate variability. In particular, Figure S8 indicates that in Malawi and Namibia, negative associations between dry-spell exposure and yield persist after accounting for seasonal rainfall. In some regions, furthermore, rainfall seasonality has a clearer effect than seasonal rainfall on yield.

Namely, delayed rainy season onset and false starts to the rainy season are detrimental to yield in South Africa, and short season length is associated with low yield in Namibia. In both of these regions, the effect of seasonal rainfall is comparatively weak.

Despite these complexities, statistically significant associations between rainfall and/or temperature variability and maize yield are evident across much of southern Africa. These findings motivate an assessment of climatic risk to yield that accounts for regional variation in both climate–yield relationships and meteorological anomalies.

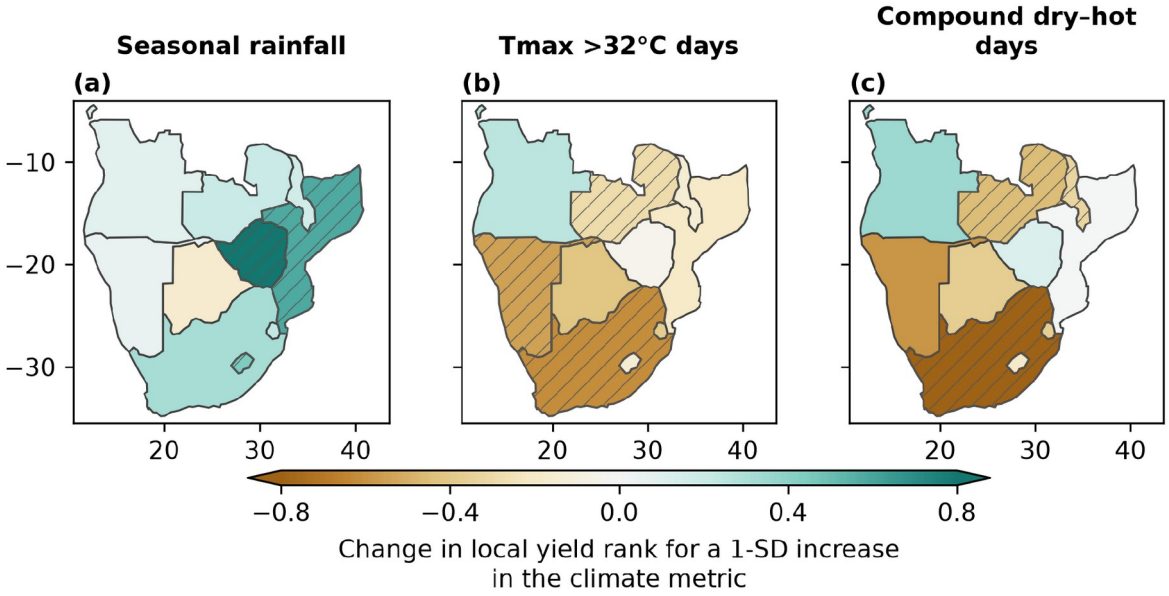


Figure 1. Links between maize yield rank and rainy-season meteorological anomalies during 1983/84–2023/24. Panels show the change in 5-year yield rank associated with a one-standard-deviation increase in (a) seasonal rainfall, accounting for hot days; (b) days with daily maximum temperature (Tmax) >32°C, accounting for rainfall; and (c) compound dry–hot days, accounting for rainfall. Light hatching denotes 95% percentile intervals excluding zero, based on 2,000 individual-season bootstrap samples, without a multiple-comparison adjustment.

3.2 El Niño impacts on maize yield risk

The sensitivity of maize yields to rainfall and temperature variability potentially exposes farmers to substantial risks during El Niño events. The spatially varying climate–yield relationships identified above provide a basis for understanding how those risks differ across southern Africa. Figure 2a and Figure S13a-c show that El Niño is associated with low yield in all countries other than Angola. Over the domain as a whole, these lower yields are associated with lower than average seasonal rainfall and a greater frequency of hot days and compound dry–hot days (Figure 2e, i and m, and Figure S13d–l). The spatial pattern of El Niño meteorological anomalies does not, however, consistently correspond to the patterns of yield impact. For example, the reduction in maize yield in South Africa during El Niño years is strong compared to other countries, despite the relatively weak rainfall teleconnection. This variability is also evident when comparing the three strongest El Niño events: South Africa had the lowest yield in 2023/2024 even though seasonal rainfall was near average. Figure 2 shows similar contrasts for other countries and variables.

These contrasts suggest that the El Niño yield response reflects both the climate anomalies experienced in each country and the country-specific sensitivity of maize yield to rainfall and heat. Figure 3 therefore decomposes the El Niño-associated yield difference into rainfall-associated and heat-associated contributions (see Supplementary Information for methodological details). The spatial pattern of these contributions broadly echoes the climate sensitivities shown in Figure 1. Replacing hot-day counts with compound dry–hot-day counts gives broadly similar results (Figure S14) - consistent with the similar spatial patterns evident in Figures 2i and m. Although compound events are associated with yield variability, their inclusion therefore makes little difference to the regional pattern of estimated El Niño contributions. It should be noted, however, that these additive models and compound metrics do not fully represent nonlinear climate–yield responses. For example, using compound-day counts represents heat exposure under dry conditions but the model assumes a linear yield response to these counts and does not explicitly account for differences in impact associated with event severity or timing within crop development. Using compound-day counts captures the co-occurrence of hazards but does not fully represent these interactions.

The residuals shown in Figure 3 and Figure S14 indicate that the primary climate metrics do not fully account for the observed El Niño-associated yield differences. To investigate these residuals further, we added dry-spell exposure, false starts, late onset, season length and within-season timing separately to the model (Figure S20). Each extension was evaluated alongside seasonal rainfall and hot-day exposure to assess its additional explanatory value. Some additions improved cross-validated yield prediction, but none produced a statistically robust reduction in the residual El Niño association. Within-season timing gave the largest estimated reduction in South Africa, although with considerable uncertainty. Overall, the additional metrics tested provide no clear explanation for the remaining association, raising the possibility that climate anomalies alone do not fully account for El Niño-associated yield deficits.

Using neutral seasons rather than all other seasons as the reference retains the main regional contrasts in estimated rainfall and heat contributions (Figures S21 and S22). Heat remains the larger estimated contribution in South Africa, Namibia and Zambia, and rainfall in Zimbabwe and Mozambique, although the neutral-reference rainfall contributions have 95% intervals

spanning zero. Residuals are more sensitive to the reference group: the South African residual remains substantial and becomes more negative, as does Zimbabwe's, whereas those in Mozambique and Malawi become close to zero. The results were also relatively insensitive to the heat-exposure definition. Specifically, using the percentage of hot days within the diagnosed season or counts within fixed local climatological windows changed estimated heat contributions by median absolute differences of 0.03 and 0.04 yield-rank units, respectively. Neither alternative produced a statistically robust reduction in residual magnitude.

To sum up, these results extend previous work on El Niño teleconnections [3] and maize yield impact [7, 8, 21] through a systematic comparison of rainfall and heat contributions across ten southern African countries. The estimated contributions reveal contrasting climatic pathways of yield risk, reflecting both the anomalies experienced during El Niño and regional differences in yield sensitivity. These analyses identify which meteorological hazards are most relevant when assessing opportunities to anticipate agricultural risk.

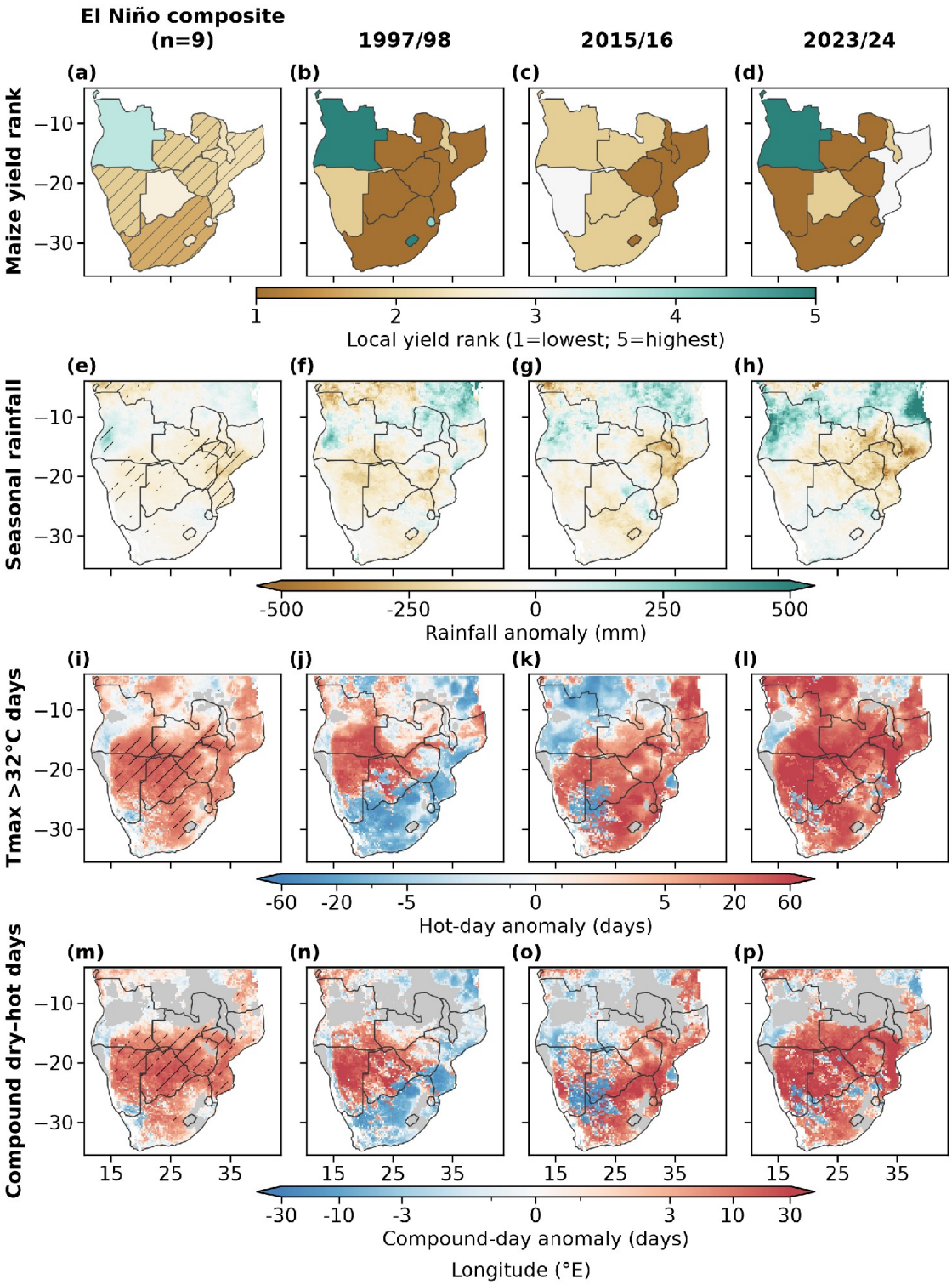


Figure 2. Maize-yield ranks and rainy-season climate anomalies during El Niño. Columns show the composite of nine moderate, strong and very strong El Niño seasons, and the three strongest events. The top row shows national FAOSTAT maize yields ranked within local five-harvest windows. Subsequent rows show seasonal rainfall, days with Tmax >32°C, and compound days with Tmax >32°C preceded by at least five consecutive days with rainfall <1 mm/day. Hatching in the composite column indicates that the pointwise 95% percentile-bootstrap interval for the El Niño-minus-other-season difference excludes zero, based on 2,000 resamples.

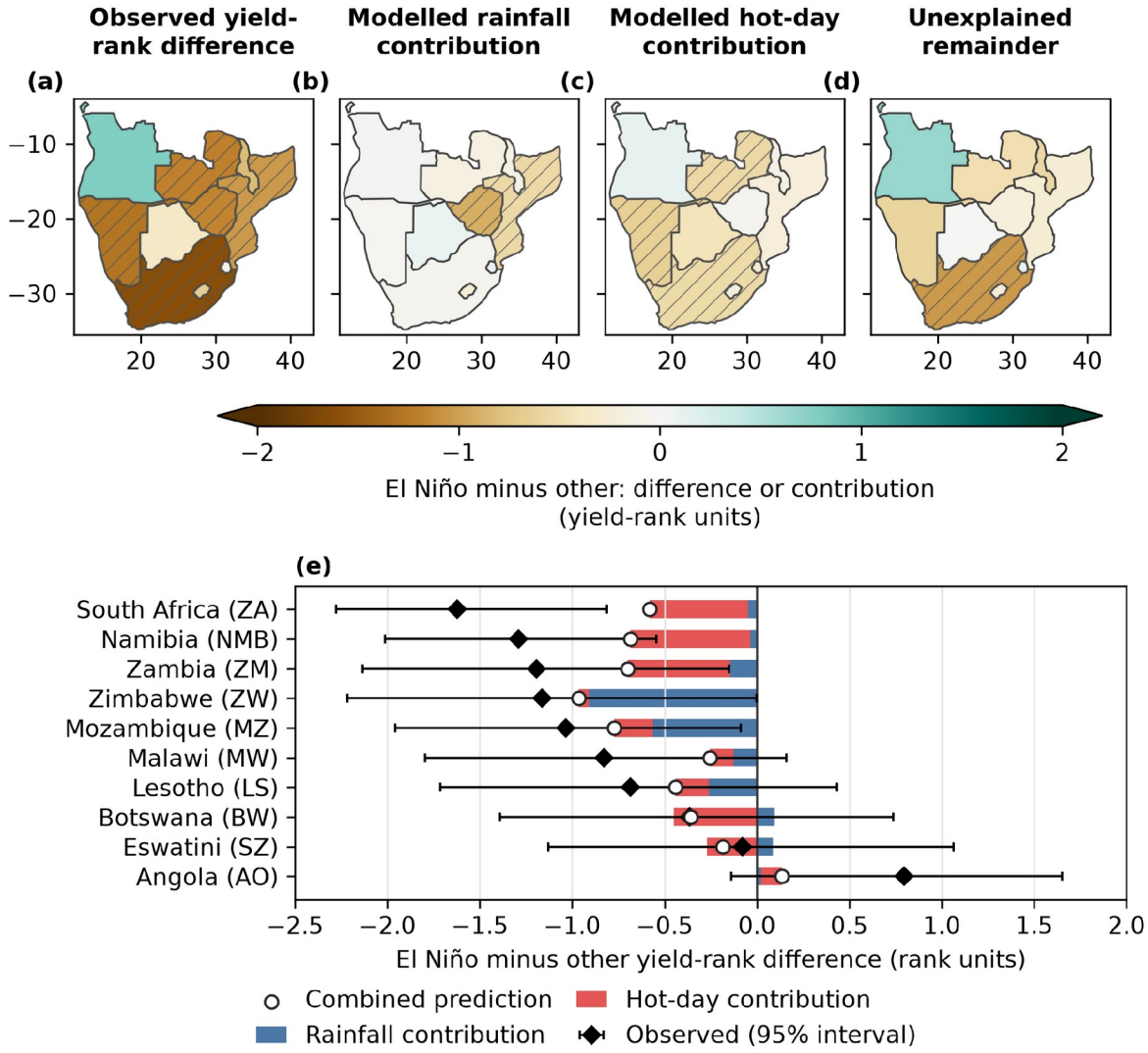


Figure 3. Rainfall and heat contributions to yield differences during El Niño. The plots compare observed and modelled national maize-yield-rank differences between nine moderate, strong and very strong El Niño seasons and all other seasons during 1983/84–2023/24. Maps show (a) the observed rank difference, (b) the rainfall-associated contribution, (c) the hot-day-associated contribution and (d) the unexplained remainder. Diagonal hatching marks a country where the corresponding 95% season-resampling bootstrap interval excludes zero, based on 2,000 resamples. Panel (e) compares the observed difference with the separate rainfall and heat contributions and their combined prediction.

3.3 Forecasting maize-relevant climate hazards

The previous analyses have demonstrated both the strong sensitivity of maize yield to temperature and precipitation, and the diversity in climatic responses to El Niño. These complexities mean that informal assessments based on historical El Niño impacts may not paint an accurate picture of risk for a given locality and year. Medium range and seasonal meteorological forecasts may offer information beyond climatology, and thus be useful for anticipatory action, provided they target metrics of relevance to crop yield.

Previous evaluations show that precipitation forecast skill is greatest at short leads and declines rapidly over subsequent weeks, including over Africa [28]. Multi-model seasonal forecast assessments, furthermore, find that skill decreases beyond the first forecast month, particularly for precipitation [29, 56]. We therefore evaluate 30-day target periods initialised at the start of the target month (0-day lead) and one month earlier (30-day lead), in order to test whether anomalous conditions can be anticipated at leads relevant to decision making. We focus on two target periods: 1-30 November and 1-30 March, chosen to represent early crop establishment and later season crop development stages (particularly flowering and grain-filling).

We selected the meteorological variables based on the analyses of yield–climate sensitivities and El Niño teleconnections: accumulated rainfall, mean maximum daily temperature (Tmax) and the number of compound dry–hot days. Tmax was selected as the primary temperature variable in preference to the count of days >32°C because it provides a general assessment of temperature forecast skill and avoids making the initial assessment dependent on the accuracy of forecasts near the 32°C threshold. The compound metric was retained because it combines the rainfall and temperature conditions most closely linked to yield impacts (Figure 1).

The results of the skill assessment are shown in Figure 4. It is evident that, at 0-day lead, the ECMWF forecast model is more effective than a historical climatological prediction in discriminating lower tercile cumulative rainfall, and upper-tercile mean daily maximum temperature and compound dry–hot-day counts in most regions. For the rainfall metric, the skill reduces to approximately climatological level for a 30-day lead in most regions for both November and March, while some skill is retained for the temperature and compound metrics.

The limited skill of the ECMWF precipitation forecasts at a 30-day lead raises the question of whether newer machine-learning weather forecasting systems offer improvements. To investigate this, the ECMWF model was compared to NeuralGCM – a machine learning system developed by Google. Figure 5 and Figure S23 reveal regional differences in performance, but neither system is consistently better or worse for subseasonal predictions.

Previous work has shown that forecast skill can vary with the large-scale climate state, potentially creating ‘windows of opportunity’ for prediction [29, 30]. We therefore compare skill during El Niño with equally sized samples of neutral and La Niña seasons. Figure 6 and Figures S24–S26 show spatial variation in both the magnitude and direction of the differences. In parts of the northern domain, March rainfall anomaly correlations at one-month lead are higher during El Niño than the mean control correlation, suggesting an opportunity to anticipate later-season rainfall anomalies. However, the limited number of El Niño events means that these patterns should be interpreted as suggestive rather than firm evidence of a systematic enhancement in skill. Sensitivity to omitting individual El Niño episodes is shown in Figure S27.

These results identify two opportunities for anticipating El Niño related risk at regional scales. Even though longer lead skill is weak across the domain as a whole, precipitation forecasts show some skill at 30-day lead for selected regions and ENSO states. For temperature, the spatially varying sensitivity of maize yield indicates where heat anomalies are likely to have the greatest impacts, and thus where the relatively greater persistence of temperature forecast skill may be most useful for regional risk assessment.

More generally, ECMWF and NeuralGCM show different spatial patterns of skill, with neither system consistently outperforming the other. Physics-based and machine-learning models represent fundamentally different approaches to prediction, so the availability of operational machine-learning systems could expand opportunities for useful forecasts. Each approach may provide information in regions or conditions where the other performs poorly.

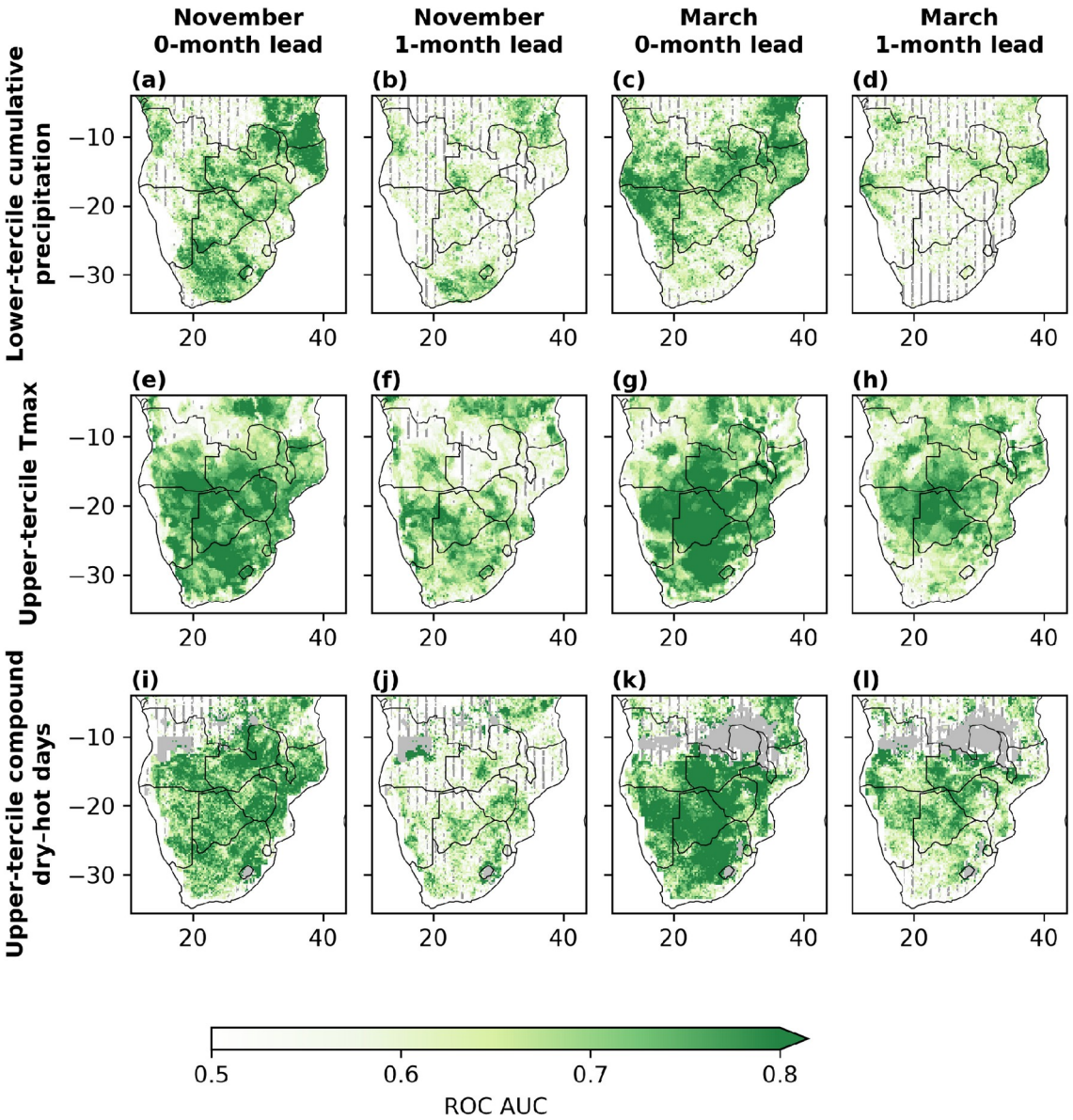


Figure 4. Skill of the ECMWF IFS for forecasting temperature and precipitation at 0 and 30 day leads. The metrics shown are ROC-AUC for lower-tercile rainfall, upper-tercile mean daily maximum temperature (Tmax) and upper-tercile compound dry–hot-day counts on the TAMSAT grid. Columns show 1–30 November and 1–30 March at 0-month and 1-month lead. November forecasts are initialised on 1 November and 1 October, respectively; March forecasts are initialised on 1 March and 1 February, respectively. Vertical hatching marks scores below 0.5. Grey denotes cells where there were insufficient observed or forecast events to calculate the ROC-AUC.

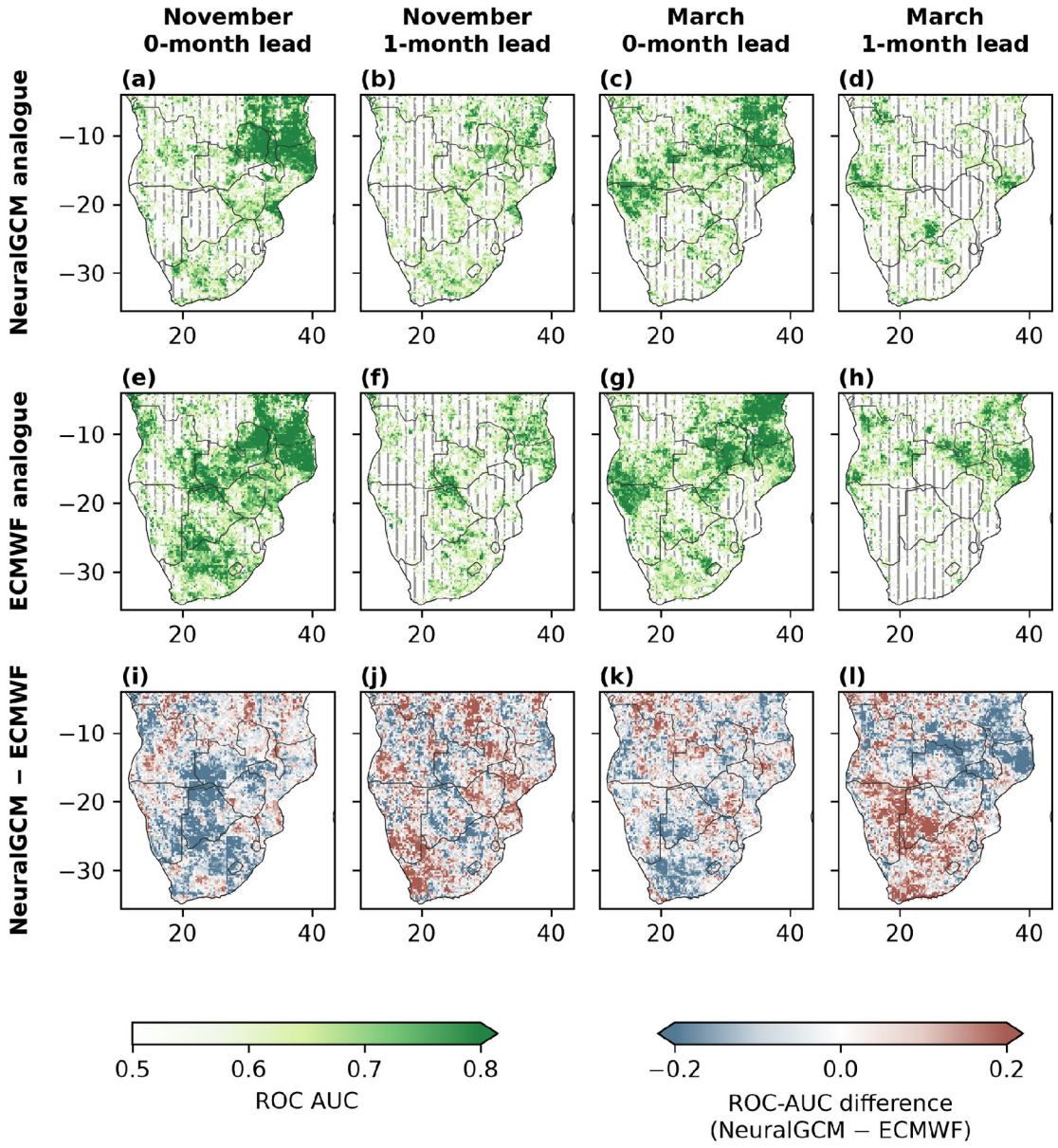


Figure 5. Comparison between ECMWF and NeuralGCM forecast skill. The metric shown is lower-tercile cumulative-precipitation ROC-AUC for NeuralGCM (top), analogue-translated ECMWF (middle) and their difference, NeuralGCM minus ECMWF (bottom). Columns show 1–30 November and 1–30 March at 0-month and 1-month lead, using 1 November/1 October and 1 March/1 February initialisations, respectively. Verification uses the 22 common years 1983–1999 and 2021–2025. Both ECMWF and NeuralGCM are downscaled using a simple analogue method.

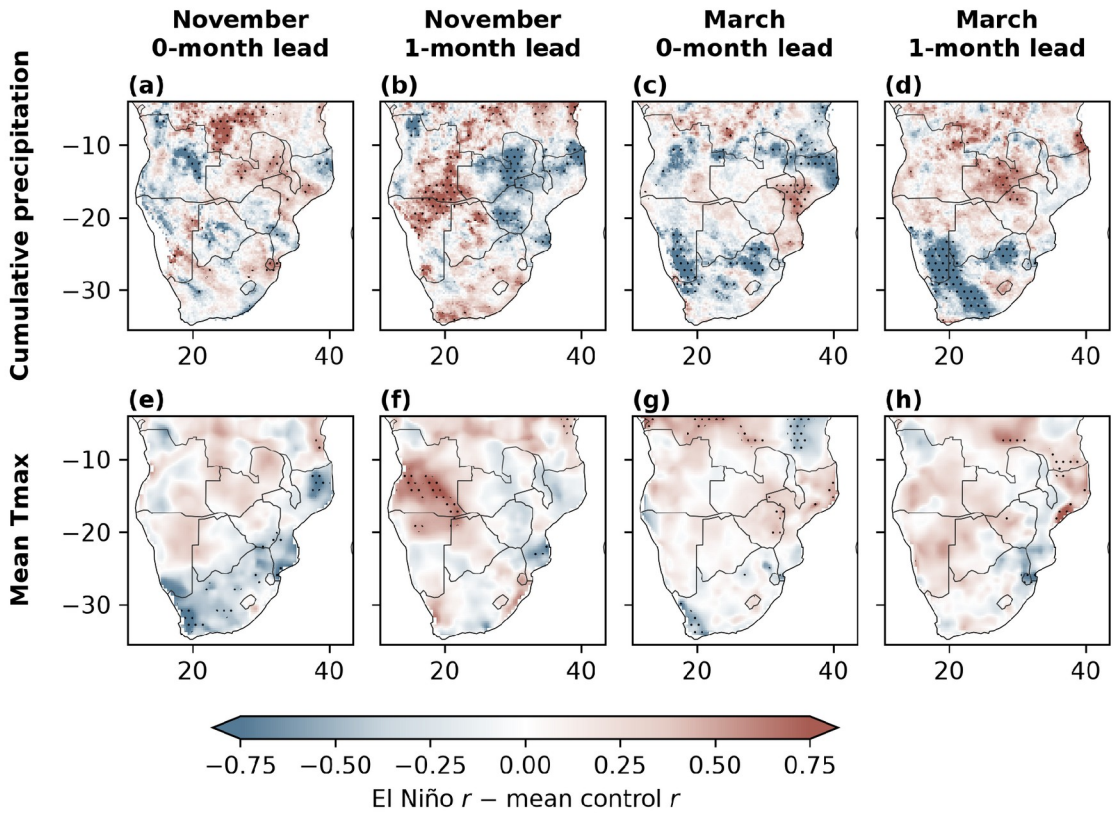


Figure 6. Effect of El Niño on forecast skill. The maps show the difference between signed El Niño anomaly correlation coefficient (ACC) and the mean ACC of 10,000 equal-sized control samples. Rows show cumulative precipitation and mean Tmax; columns show November and March at 0-month and 1-month lead, using same-month and preceding-month first-day initialisations (1 November/1 October and 1 March/1 February, respectively). Raw ECMWF ensemble-mean cumulative precipitation and mean Tmax are verified against TAMSAT and CPC for 1–30 November and 1–30 March at both leads. Dots mark cells where El Niño r lies outside the pointwise central 95% control-reference range (2.5th–97.5th percentiles of 10,000 subsamples).

4 Conclusions

El Niño-related maize yield risk reflects both the climate anomalies experienced and regional differences in sensitivity to rainfall and heat. Across the ten countries studied, rainfall deficits dominate the estimated climatic contribution in Zimbabwe and Mozambique, whereas heat contributes more strongly in several other countries, including South Africa, Namibia and Zambia. These contrasts highlight the importance of interpreting the agricultural impact of meteorological anomalies within their local climatic context. Present-day heat exposure also offers a possible analogue for conditions that could become more widespread under climate change, increasing the importance of heat-related yield risk [57].

The rainfall and heat metrics investigated do not fully account for the observed El Niño-associated yield deficits. The additional climate metrics tested provide no robust reduction in this residual, although within-season timing may contribute in South Africa. While other

climatic explanations remain possible, these findings motivate investigation of behavioural and economic pathways. These include changes in agricultural investment in anticipation of El Niño [27], and possible market influences on agricultural input use [58] and insurance prices [59].

The contrasting climatic pathways nevertheless identify regional opportunities for early warning. Where heat contributes substantially to yield deficits, the more persistent skill of mean daily maximum temperature forecasts offers additional information for anticipating impact-relevant adverse conditions, even when rainfall forecast skill is limited. Indications of enhanced March rainfall forecast skill during El Niño in northern parts of the domain also suggest scope to anticipate later season water stress. Despite generally limited precipitation forecast skill at the spatial and temporal scales relevant to agricultural decisions, these specific sources of skill indicate the potential for valuable warning during El Niño events.

5 References

1. Shiferaw, B., et al., *Crops that feed the world 6. Past successes and future challenges to the role played by maize in global food security.* Food security, 2011. **3**(3): p. 307–327.
2. Mutengwa, C.S., P. Mnkeni, and A. Kondwakwenda, *Climate-smart agriculture and food security in Southern Africa: A review of the vulnerability of smallholder agriculture and food security to climate change.* Sustainability, 2023. **15**(4): p. 2882.
3. Cai, W., et al., *Climate impacts of the El Niño–Southern oscillation in Africa.* Nature Reviews Earth & Environment, 2025. **6**(8): p. 503–520.
4. Mason, S.J., *El Niño, climate change, and Southern African climate.* Environmetrics: The official journal of the International Environmetrics Society, 2001. **12**(4): p. 327–345.
5. Nicholson, S.E. and J. Kim, *The relationship of the El Niño–Southern oscillation to African rainfall.* International Journal of Climatology: A Journal of the Royal Meteorological Society, 1997. **17**(2): p. 117–135.
6. Mpheshea, L.E., R.C. Blamey, and C.J. Reason, *The influence of ENSO-type on rainfall characteristics over southern Africa during the austral summer.* Climate Dynamics, 2025. **63**(3): p. 161.
7. Cane, M.A. and G. Eshel, *Forecasting Zimbabwean maize yield using eastern equatorial Pacific sea surface temperature.* Nature, 1994. **370**(6486).
8. Phillips, J., M. Cane, and C. Rosenzweig, *ENSO, seasonal rainfall patterns and simulated maize yield variability in Zimbabwe.* Agricultural and Forest Meteorology, 1998. **90**(1-2): p. 39–50.
9. Sazib, N., L.E. Mladenova, and J.D. Bolten, *Assessing the impact of ENSO on agriculture over Africa using earth observation data.* Frontiers in Sustainable Food Systems, 2020. **4**: p. 509914.
10. Muza, O., *El Nino-Southern Oscillation influences on food security.* J. Sustain. Dev, 2017. **10**(5): p. 268–279.
11. Stige, L.C., et al., *The effect of climate variation on agro-pastoral production in Africa.* Proceedings of the National Academy of Sciences, 2006. **103**(9): p. 3049–3053.
12. Manatsa, D., G. Mukwada, and L. Makaba, *ENSO shifts and their link to Southern Africa surface air temperature in summer: D. Manatsa et al.* Theoretical and Applied Climatology, 2018. **132**(3): p. 727–738.
13. Shiferaw, B., et al., *Managing vulnerability to drought and enhancing livelihood resilience in sub-Saharan Africa: Technological, institutional and policy options.* Weather and climate extremes, 2014. **3**: p. 67–79.

14. Connolly-Boutin, L. and B. Smit, *Climate change, food security, and livelihoods in sub-Saharan Africa.* Regional Environmental Change, 2016. **16**(2): p. 385–399.
15. Magrath, J., *Entering Uncharted Waters: El Niño and the threat to food security*. 2015: Oxfam International.
16. Programme, W.F. *WFP races to cushion people from looming drought in Southern Africa in largest cash payout to date* 2023 [cited 2026 09/23/2026]; Available from: https://www.wfp.org/news/wfp-races-cushion-people-looming-drought-southern-africa-largest-cash-payout-date.
17. Taiz, L., et al., *Plant physiology and development*. 2015.
18. Agrios, G.N., *Plant pathology*. 2005: Elsevier.
19. Wahid, A., et al., *Heat tolerance in plants: an overview.* Environmental and experimental botany, 2007. **61**(3): p. 199–223.
20. Iizumi, T., et al., *Impacts of El Niño Southern Oscillation on the global yields of major crops.* Nature communications, 2014. **5**(1): p. 3712.
21. Cook, B.I., et al., *Investigating the strength and variability of El Niño–Southern oscillation teleconnections to hydroclimate and maize yields in Southern and East Africa.* Journal of Hydrometeorology, 2024. **25**(1): p. 257–275.
22. Bradshaw, C.D., et al., *Unprecedented climate extremes in South Africa and implications for maize production.* Environmental Research Letters, 2022. **17**(8): p. 084028.
23. Capotondi, A., et al., *Understanding ENSO diversity.* Bulletin of the American Meteorological Society, 2015. **96**(6): p. 921–938.
24. Kug, J.-S., F.-F. Jin, and S.-I. An, *Two types of El Niño events: cold tongue El Niño and warm pool El Niño.* Journal of climate, 2009. **22**(6): p. 1499–1515.
25. Blamey, R., et al., *The role of regional circulation features in regulating El Niño climate impacts over southern Africa: A comparison of the 2015/2016 drought with previous events.* International Journal of Climatology, 2018. **38**(11): p. 4276–4295.
26. Lyon, B. and S.J. Mason, *The 1997–98 summer rainfall season in southern Africa. Part I: Observations.* Journal of Climate, 2007. **20**(20): p. 5134–5148.
27. de Perez, E.C., et al., *Detectable use of ENSO information on crop production in Southern Africa.* Climate services, 2024. **36**: p. 100514.
28. de Andrade, F.M., et al., *Subseasonal precipitation prediction for Africa: forecast evaluation and sources of predictability.* Weather and Forecasting, 2021. **36**(1): p. 265–284.
29. Young, H.R. and N.P. Klingaman, *Skill of seasonal rainfall and temperature forecasts for East Africa.* Weather and Forecasting, 2020. **35**(5): p. 1783–1800.
30. Mariotti, A., et al., *Windows of opportunity for skillful forecasts subseasonal to seasonal and beyond.* Bulletin of the American Meteorological Society, 2020. **101**(5): p. E608–E625.
31. Boult, V.L., et al., *Towards drought impact-based forecasting in a multi-hazard context.* Climate Risk Management, 2022. **35**.
32. Kochkov, D., et al., *Neural general circulation models for weather and climate.* Nature, 2024. **632**(8027): p. 1060–1066.
33. Yuval, J., et al., *Neural general circulation models optimized to predict satellite-based precipitation observations.* arXiv preprint arXiv:2412.11973, 2024.
34. Hoell, A. and J. Eischeid, *On the interpretation of seasonal Southern Africa precipitation prediction skill estimates during Austral summer: A. Hoell, J. Eischeid.* Climate Dynamics, 2019. **53**(11): p. 6769–6783.
35. Rowell, D.P., *Simulating SST teleconnections to Africa: What is the state of the art?* Journal of Climate, 2013. **26**(15): p. 5397–5418.
36. Lyon, B., *The strength of El Niño and the spatial extent of tropical drought.* Geophysical Research Letters, 2004. **31**(21).

37. Cairns, J.E., et al., *Identification of drought, heat, and combined drought and heat tolerant donors in maize.* Crop science, 2013. **53**(4): p. 1335–1346.
38. Lee, D., et al., *HarvestStat Africa–harmonized subnational crop statistics for sub-Saharan Africa.* Scientific Data, 2025. **12**(1): p. 690.
39. Zhang, W., et al., *AHAD: African major crops harvested area dataset for the years of 2000, 2010, and 2020.* Scientific Data, 2025. **12**(1): p. 1691.
40. Maidment, R.I., et al., *A new, long-term daily satellite-based rainfall dataset for operational monitoring in Africa.* Scientific Data, 2017. **4**.
41. Maidment, R.I., et al., *The 30-year TAMSAT African rainfall climatology and time-series (TARCAT) dataset.* Journal of Geophysical Research: Atmospheres, 2014. **119**(18): p. 10619–10644.
42. Tarnavsky, E., et al., *Extension of the TAMSAT satellite-based rainfall monitoring over Africa and from 1983 to present.* Journal of Applied Meteorology and Climatology, 2014. **53**(12): p. 2805–2822.
43. Funk, C., et al., *The climate hazards infrared precipitation with stations—a new environmental record for monitoring extremes.* Scientific data, 2015. **2**(1): p. 1–21.
44. Huffman, G.J., et al., *NASA global precipitation measurement (GPM) integrated multi-satellite retrievals for GPM (IMERG).* Algorithm Theoretical Basis Document (ATBD) Version, 2018. **4**.
45. Hersbach, H., et al., *The ERA5 global reanalysis.* Quarterly Journal of the Royal Meteorological Society, 2020. **146**(730): p. 1999–2049.
46. Xie, P., M. Chen, and W. Shi. *CPC unified gauge-based analysis of global daily precipitation*. in *Preprints, 24th Conf. on Hydrology, Atlanta, GA, Amer. Meteor. Soc*. 2010.
47. Chen, M., et al., *Assessing objective techniques for gauge-based analyses of global daily precipitation.* Journal of Geophysical Research: Atmospheres, 2008. **113**(D4).
48. Maidment, R.I., R.P. Allan, and E. Black, *Recent observed and simulated changes in precipitation over Africa.* Geophysical Research Letters, 2015. **42**(19): p. 8155–8164.
49. Maidment, R., et al., *TAMSAT*, in *Satellite Precipitation Measurement*, V. Levizzani, et al., Editors. 2020, Springer. p. 393–407.
50. Liu, R., et al., *Global-scale ERA5 product precipitation and temperature evaluation.* Ecological Indicators, 2024. **166**: p. 112481.
51. Johnson, S.J., et al., *SEAS5: the new ECMWF seasonal forecast system.* Geoscientific Model Development, 2019. **12**(3): p. 1087–1117.
52. Liebmann, B., et al., *Seasonality of African precipitation from 1996 to 2009.* Journal of Climate, 2012. **25**(12): p. 4304–4322.
53. Dunning, C.M., E.C.L. Black, and R.P. Allan, *The onset and cessation of seasonal rainfall over Africa.* Journal of Geophysical Research: Atmospheres, 2016. **121**(19): p. 11405–11424.
54. Najafi, E., et al., *Understanding the changes in global crop yields through changes in climate and technology.* Earth's Future, 2018. **6**(3): p. 410–427.
55. Abate, T., et al., *Factors that transformed maize productivity in Ethiopia: T. Abate et al.* Food security, 2015. **7**(5): p. 965–981.
56. Lavers, D., L. Luo, and E.F. Wood, *A multiple model assessment of seasonal climate forecast skill for applications.* Geophysical research letters, 2009. **36**(23).
57. Lobell, D.B., et al., *Nonlinear heat effects on African maize as evidenced by historical yield trials.* Nature climate change, 2011. **1**(1): p. 42–45.
58. Oyinbo, O., et al., *Digital extension, price risk, and farm performance: experimental evidence from Nigeria.* American Journal of Agricultural Economics, 2022. **104**(2): p. 831–852.
59. Osgood, D., et al., *Integrating seasonal forecasts and insurance for adaptation among subsistence farmers: The case of Malawi*, in *Policy Research Working Paper*,

W. Bank, Editor. 2008 Washington DC.

Acknowledgments

This work is the National Centre for Atmospheric Science through the NERC National Capability International Programmes Award (NC/X006263/1) [E.B.]; the AI Collaborative: Food Security, funded by Google.org [E.B, P.F.].

Data and code availability statement

All third-party datasets used in this study are publicly available, subject to their respective data policies and licence conditions. TAMSAT v3.1 daily rainfall estimates are available from the University of Reading TAMSAT data service. CPC daily maximum temperature and Unified precipitation data are available from the NOAA Physical Sciences Laboratory (temperature; precipitation). Additional datasets used for sensitivity analyses include CHIRPS v3-rnl, provided by the University of California, Santa Barbara Climate Hazards Center; IMERG Final V07B, provided by NASA; and ERA5 reanalysis, available through the Copernicus Climate Data Store. National maize-yield records are available from FAOSTAT, and subnational crop statistics from HarvestStat Africa. The African Harvested Area Dataset (AHAD), used to define the maize-growing mask, is available from Zenodo. Oceanic Niño Index values used to classify seasons are available from the NOAA Climate Prediction Center. ECMWF SEAS5.1 ensemble hindcasts are available through the Copernicus Climate Data Store, subject to the applicable licence conditions. The precipitation-optimised, 2.8° NeuralGCM checkpoint used to generate the hindcasts in this study is publicly available from Google under the Creative Commons Attribution–ShareAlike 4.0 International licence (CC BY-SA 4.0), through the NeuralGCM checkpoint repository.

The code used for carrying out the analysis and preparing the figures is available on reasonable request from the corresponding author.

AI use disclosure

During this study, the authors used OpenAI's ChatGPT and Codex to assist with developing and checking analysis code, preparing figures and grammar/style checking. The authors reviewed the AI-assisted code and figures and take full responsibility for the study's methods, results and conclusions.

Conflict of interest statement

The authors declare no conflicts of interest.

Supplementary Information

Observations and exposure definitions

Additional details of the datasets used

Table S1. Datasets used in the analysis.

Dataset name and abbreviation	Resolution	Notes	URL/source	Citation
FAOSTAT country yields (FAOSTAT)	Annual; country-level (no gridded spatial resolution)	National yield records aligned to the 1983/84–2023/24 analysis seasons using harvest year minus one.	FAO data portal: http://faostat.fao.org/	FAOSTAT; accessed 2026.
HarvestStat Africa (HarvestStat)	Annual; administrative units (ADM1/ADM2, varying by country)	Harmonised subnational crop statistics for supplementary analyses of regional yield–climate relationships.	https://doi.org/10.1038/s41597-025-05001-z	Lee et al. (2025)
Africa Harvested Area Database (AHAD)	5 arcmin; 2000, 2010, 2020	Maize harvested-area maps used to construct the fixed crop mask.	https://doi.org/10.5281/zenodo.15182820	Zhang et al. (2025).
TAMSAT v3.1 (TAMSAT)	0.25° provider product used; native product 0.0375°; daily	Satellite-based rainfall estimates derived from historically calibrated Meteosat infrared imagery and rain-gauge observations; primary rainfall dataset.	https://www.tamsat.org.uk/data/	Maidment et al. (2017); Tarnavsky et al. (2014); Maidment et al. (2014).
CHIRPS v3-rnl (CHIRPS)	0.25° daily product used	Satellite-based rainfall estimates blended with station observations, used for rainfall-product sensitivity tests.	https://www.chc.ucsb.edu/data/chirps	Funk et al. (2015).
IMERG Final V07B (IMERG)	0.1° (~10 km); 30-min native data, aggregated daily	Multi-satellite precipitation estimates from the Global Precipitation Measurement mission, used for common-period rainfall sensitivity tests.	https://gpm.nasa.gov/data-access/downloads/gpm	Huffman et al. (2018).
ERA5 reanalysis (ERA5)	0.25° (~31 km); hourly, aggregated daily	Global atmospheric reanalysis combining model forecasts with observations; used for rainfall and temperature product-sensitivity checks.	https://cds.climate.copernicus.eu/datasets/reanalysis-era5-single-levels	Hersbach et al. (2020).

Dataset name and abbreviation	Resolution	Notes	URL/source	Citation
CPC Unified precipitation (CPC)	0.5°; daily	Gauge-based precipitation analysis used for rainfall-product sensitivity checks.	https:// psl.noaa.gov/	Xie et al. (2010).
CPC Global Temperature (CPC)	0.5°; daily	Station-based daily maximum temperature analysis; primary temperature dataset.	https:// psl.noaa.gov/ data/gridded/ data.cpc.globaltemp.html	NOAA CPC; obtained through NOAA PSL.

The mean growing-season climate is shown below, followed by the maize mask, season diagnosis and metric definitions.

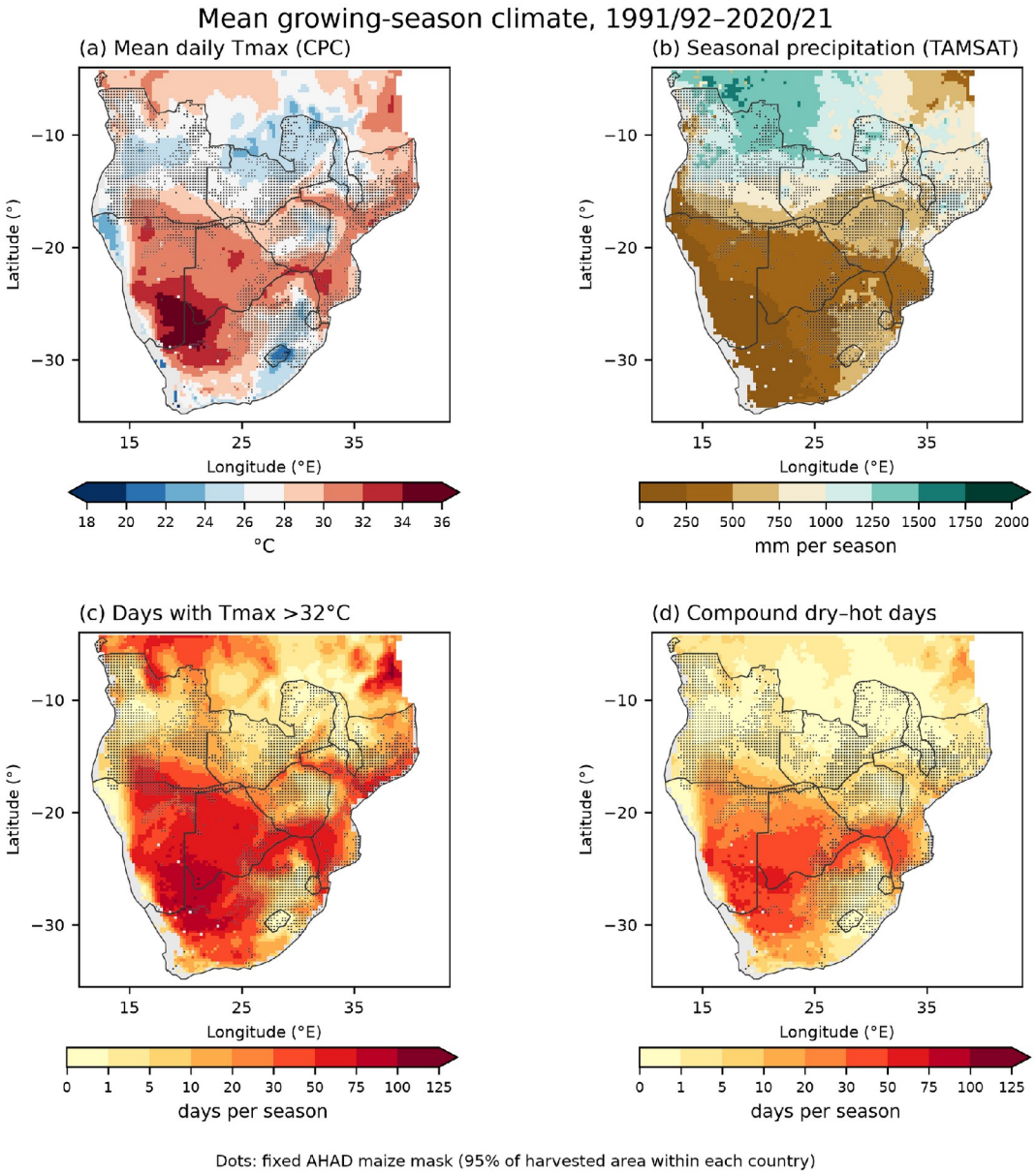


Figure S1. Mean growing-season climate over southern Africa during 1991/92–2020/21: (a) mean daily maximum temperature (Tmax; CPC); (b) total seasonal precipitation (TAMSAT); (c) number of days with Tmax >32°C; and (d) number of compound dry–hot days, defined as days with Tmax >32°C immediately preceded by at least five consecutive days with rainfall <1 mm day^{-1}. Growing seasons are approximated by the locally diagnosed TAMSAT rainy season for each year, with climatological windows used when annual timing is unavailable. Maps show the equally weighted mean of annual seasonal metrics on the common 0.25° grid. All panels use the same valid seasons at each cell, with at least 25 of the 30 seasons required. The full regional climate fields are shown; dots mark the fixed AHAD maize mask retaining 95% of the mean normalised harvested-area distribution within each country (2000, 2010 and 2020); compound counts represent qualifying days, not separate spells.

Masking on maize growing regions

We restricted the climate–yield analysis to areas of substantial maize production using a fixed maize mask derived from the Africa Harvested Area Database (AHAD) [1]. Harvested-area rasters for 2000, 2010 and 2020 were conservatively regridded to the 0.25° climate grid. For each country, the harvested-area distribution in each reference year was normalised and the three distributions were averaged. Grid cells were ranked by the resulting mean distribution, and the smallest set containing 95% of the mean maize harvested area was retained. This fixed mask was applied to all years and climate variables in the yield analyses; country-level metrics were then calculated over the retained cells using cosine-latitude area weights.

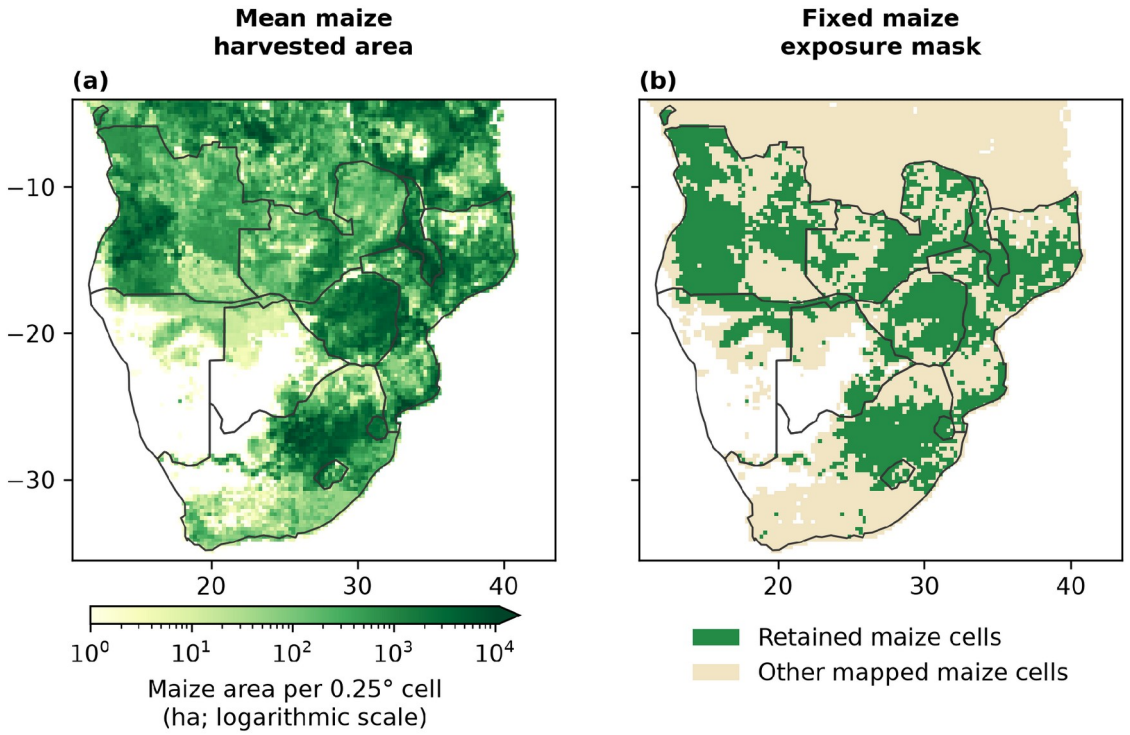


Figure S2. Maize coverage and the fixed spatial mask used for FAOSTAT country-level climate exposure. (a) Mean maize harvested area per 0.25° grid cell across the AHAD maps for 2000, 2010 and 2020, conservatively aggregated from 5-arcminute harvested hectares. (b) Retained maize cells (green) and other cells with mapped maize (pale tan) used for the masking.

Rainfall season diagnosis

Rainfall seasonality was diagnosed separately for each climate grid cell using a Dunning-style rainfall-season algorithm. Daily rainfall was first expressed on a 365-day no-leap calendar, and the climatological daily rainfall cycle was calculated from the available record. Harmonic analysis was then used to distinguish predominantly unimodal from bimodal rainfall regimes. At each grid cell, the rainy season was identified from the seasonal evolution of cumulative rainfall, giving estimates of onset and cessation. The season calendar begins on 1 August. Where more than one climatological rainy season was identified, the target season was selected as the one with greatest overlap with the November–March window, targeting the main austral-summer rains.

The resulting climatological season definitions were used to calculate year-specific onset, cessation and season length where the annual rainfall record supported a valid diagnosis. Seasonal rainfall totals, hot-day counts and compound dry–hot-day counts were calculated within these locally varying rainy-season windows. Where annual onset or cessation could not be diagnosed reliably, rainfall and heat-exposure metrics used the corresponding grid-cell climatological season window; timing-based metrics such as late onset, false starts and season length were treated as missing. This approach allows climate exposure to be measured over agriculturally relevant seasons while retaining spatial variation in rainfall timing across the study region.

Figure S3 compares maps of rainy-season onset and cessation across all the rainfall datasets included in this study.

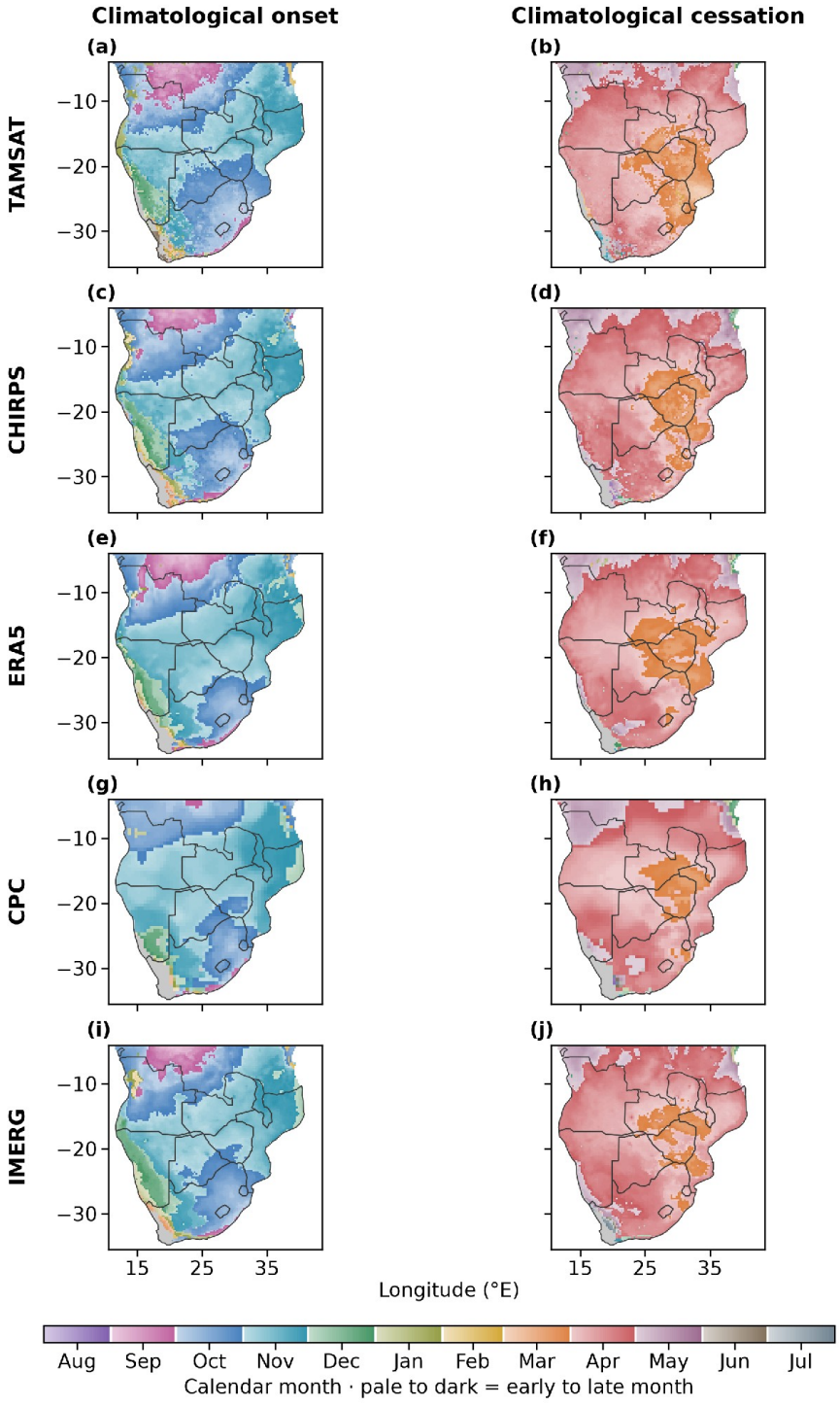


Figure S3. Climatological onset (left) and cessation (right) of the target austral-summer rainy season, diagnosed independently from TAMSAT, CHIRPS v3-rnl, ERA5, CPC precipitation and IMERG Final V07B. All products use daily climatologies from 1 August 1998 to 31 July 2024 (1998/99–2023/24) on the TAMSAT 0.25° grid.

Definitions of agriculturally relevant meteorological metrics

The meteorological metrics used in the study are defined in Table S2 below.

Table S2. Definitions and country-level measures for the meteorological metrics used in this study.

Candidate	Definition	Country measure
Seasonal rainfall	Total rainfall accumulated over the diagnosed local rainy season.	Area-mean seasonal total
Mean Tmax	Mean daily maximum temperature over the specified assessment period.	Area-mean temperature
Hot days	Number of days during the diagnosed rainy season with daily maximum temperature exceeding 32°C.	Area-mean number of days
Compound dry–hot days	Number of days during the diagnosed rainy season with daily maximum temperature above 32°C, immediately preceded by at least five consecutive days with rainfall below 1 mm/day.	Area-mean number of days
DSI5	Days belonging to dry spells of at least five consecutive days, each with rainfall below 1 mm/day, within the diagnosed rainy season.	Area-mean index (unit is days)
False starts	At least seven consecutive days with rainfall below 1 mm/day during days 1–30 after diagnosed annual onset, restricted to the season. Requires valid annual timing.	Percentage of maize-mask area affected
Late onset	Diagnosed annual onset strictly later than the local upper-tercile onset date from 1991–2020. Requires valid annual timing and threshold.	Percentage of maize-mask area affected
Season length	Duration of the annually diagnosed rainy season, inclusive of onset and cessation. Requires valid annual timing.	Area-mean days

Sensitivity to the observational climate product

Rainfall composites are compared across observational products on matched support, followed by the CPC–ERA5 hot-day comparison.

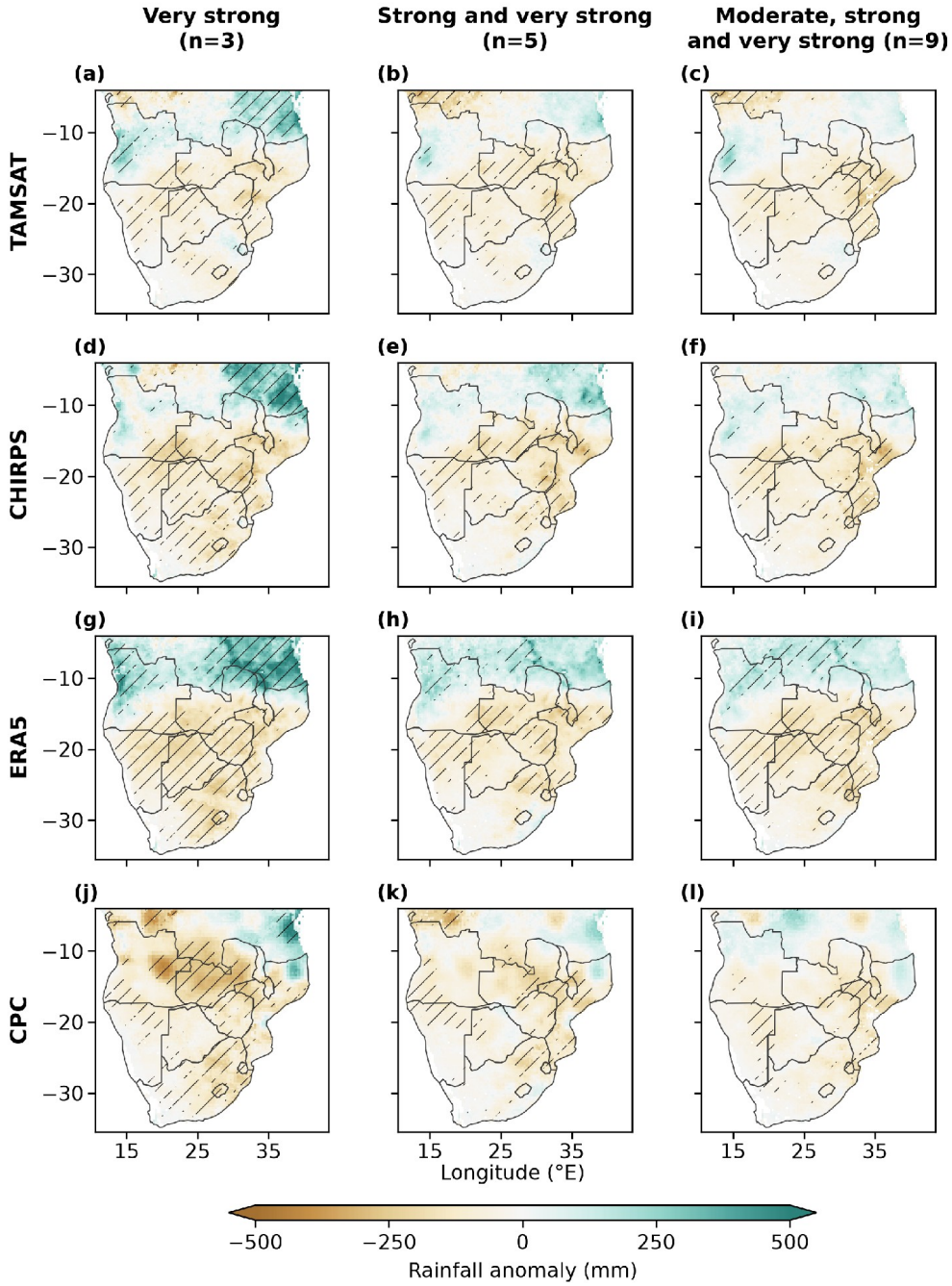


Figure S4. Rainfall-product sensitivity of El Niño rainy-season rainfall composites. Rows show TAMSAT, CHIRPS v3-rnl, ERA5 and CPC precipitation; columns show the three very strong, five strong and very strong, and nine moderate, strong and very strong events. Anomalies are differences from the mean of seasons outside the respective event group during 1983/84–2023/24. All products use the same TAMSAT-derived annual rainy-season windows, with climatological fallback, and the same 0.25° grid. At each cell, only seasons with valid totals in every displayed product enter the calculation. Hatching indicates pointwise 95% percentile-bootstrap intervals excluding zero, from 2,000 separate resamples of selected and other seasons.

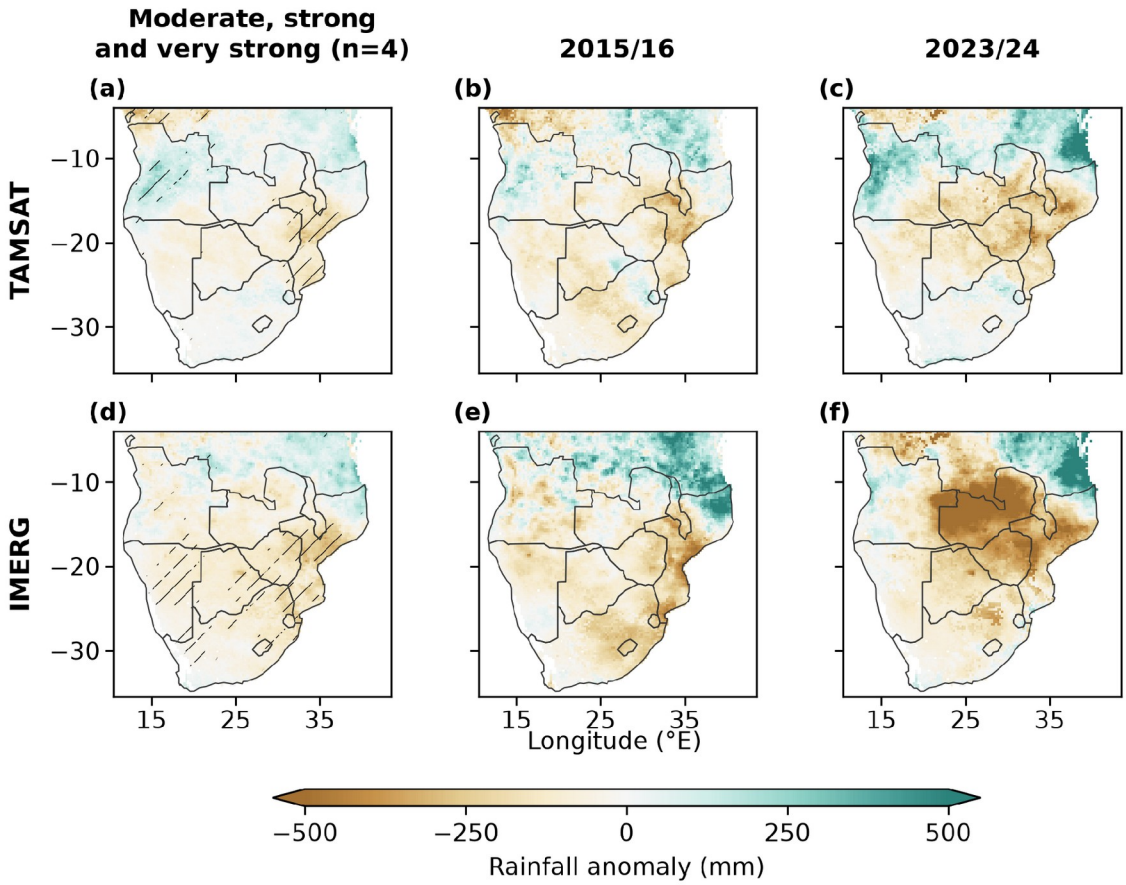


Figure S5. Common-period comparison of TAMSAT and IMERG Final V07B rainy-season rainfall anomalies during 1998/99–2023/24. The first column averages four moderate, strong and very strong El Niño seasons; the remaining columns show 2015/16 and 2023/24. All columns use the mean of seasons outside the four-event set as their reference. Season windows, grid and finite-year support are matched between products. Hatching in the composite column denotes pointwise 95% percentile-bootstrap intervals excluding zero, using 2,000 resamples within each group; individual-event maps are descriptive and have no inference markings.

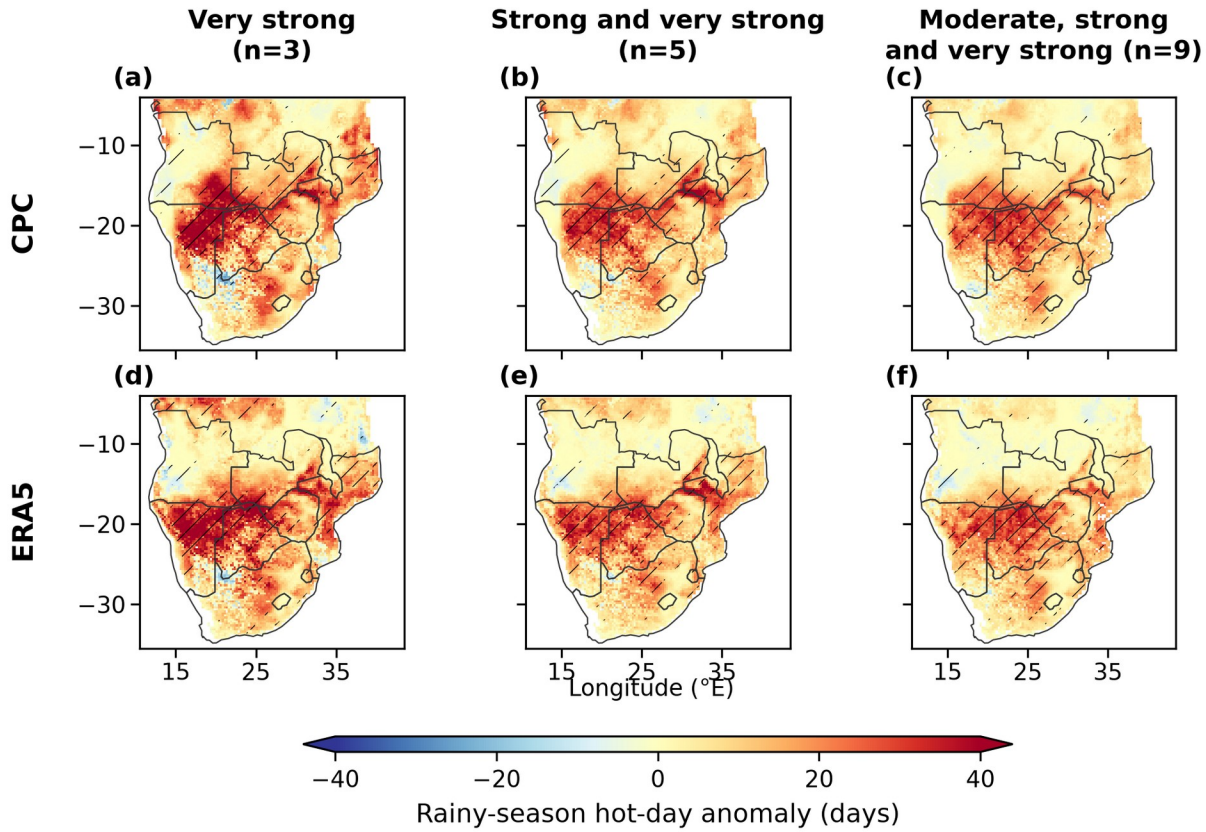


Figure S6. Comparison of CPC and ERA5 rainy-season hot-day composites during El Niño. Rows show CPC and ERA5 daily maximum temperature; columns show the very strong, strong and very strong, and moderate, strong and very strong El Niño event groups. Values are anomalies in the number of rainy-season days with Tmax >32°C relative to seasons outside the selected event group during 1983/84–2023/24. Both products use the same TAMSAT-derived annual rainy-season windows, common 0.25° grid and analysis-domain mask. Hatching indicates that the pointwise 95% percentile-bootstrap interval for the El Niño-minus-other-season difference excludes zero, based on 2,000 resamples. The figure compares the temperature products; it does not test the significance of differences between CPC and ERA5.

Climate–yield relationships and sensitivity estimates

The following figures show single-variable explanatory power, candidate rainfall metrics and subnational relationships. The coefficient-robustness checks then assess temporal sampling and the yield measure.

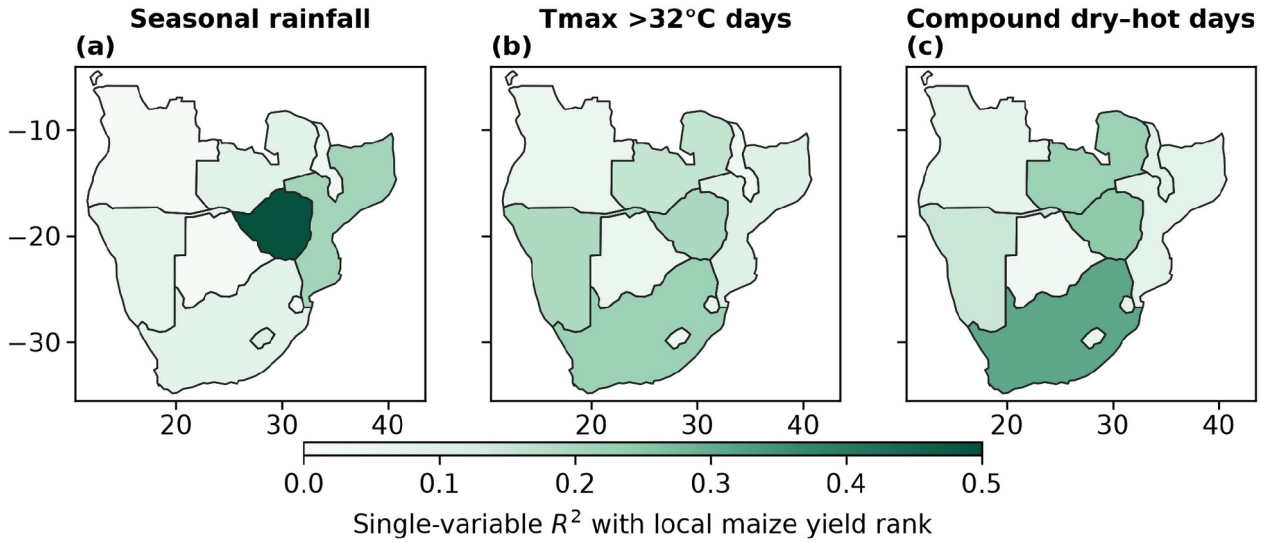


Figure S7. Country-level single-variable R2 (variance explained) between 5-year maize-yield ranks and (a) seasonal rainfall, (b) rainy-season days with Tmax >32°C and (c) compound dry–hot days. Values are squared Pearson correlations calculated from complete local five-harvest rank windows and national time series (climate time series masked using the AHAD mask shown in Figure S2).

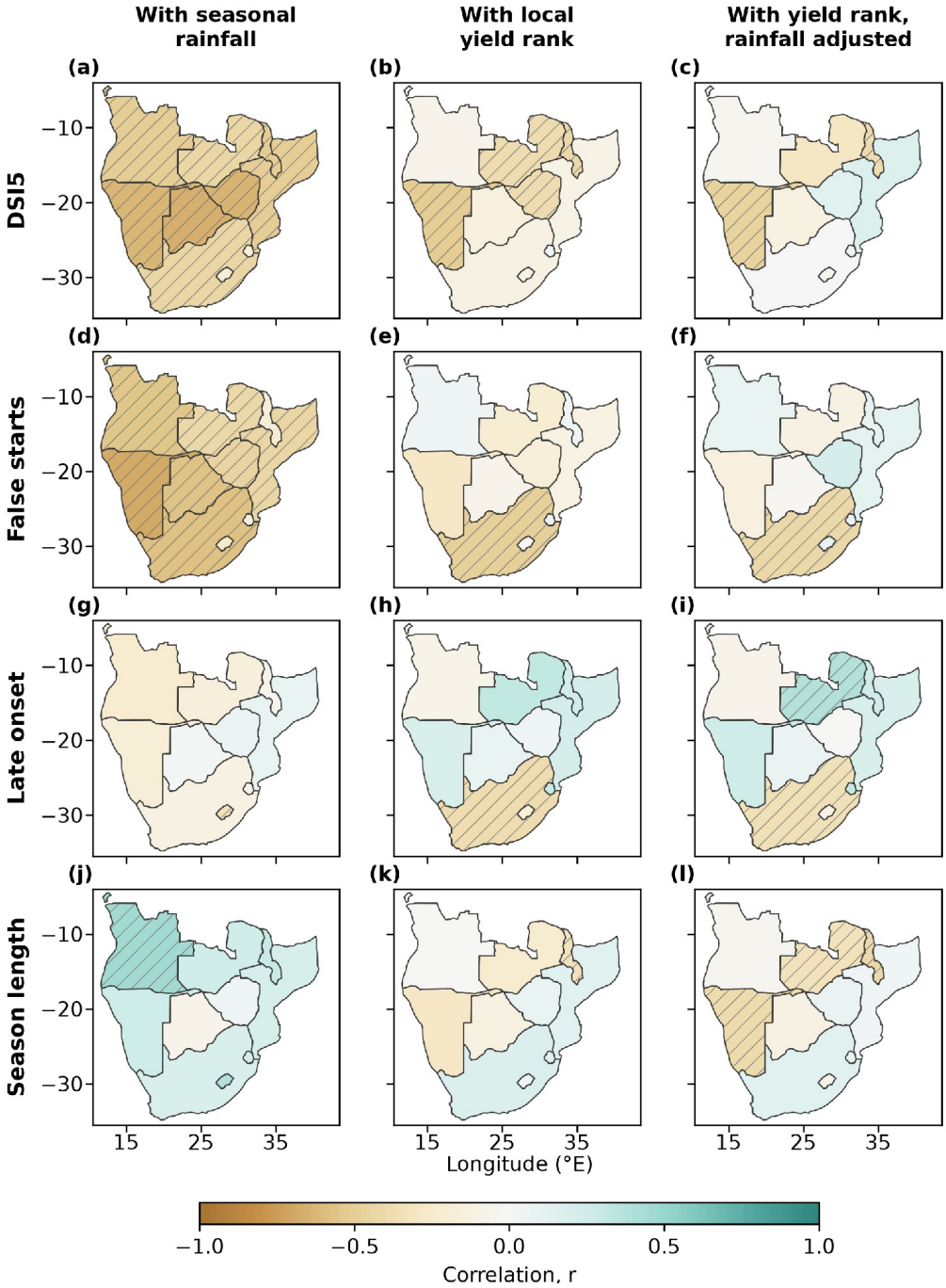


Figure S8. Candidate rainy-season metrics and their relationships with seasonal rainfall and maize yield. Rows show DSI5, false-start affected area, late-onset affected area and rainy-season length. Columns show: signed correlations with seasonal rainfall; correlations with national FAOSTAT maize yield ranks; and partial correlations with yield ranks after linearly removing seasonal rainfall from both variables. Hatching indicates a pointwise 95% percentile-bootstrap interval excluding zero, based on 2,000 paired resamples of complete seasons.

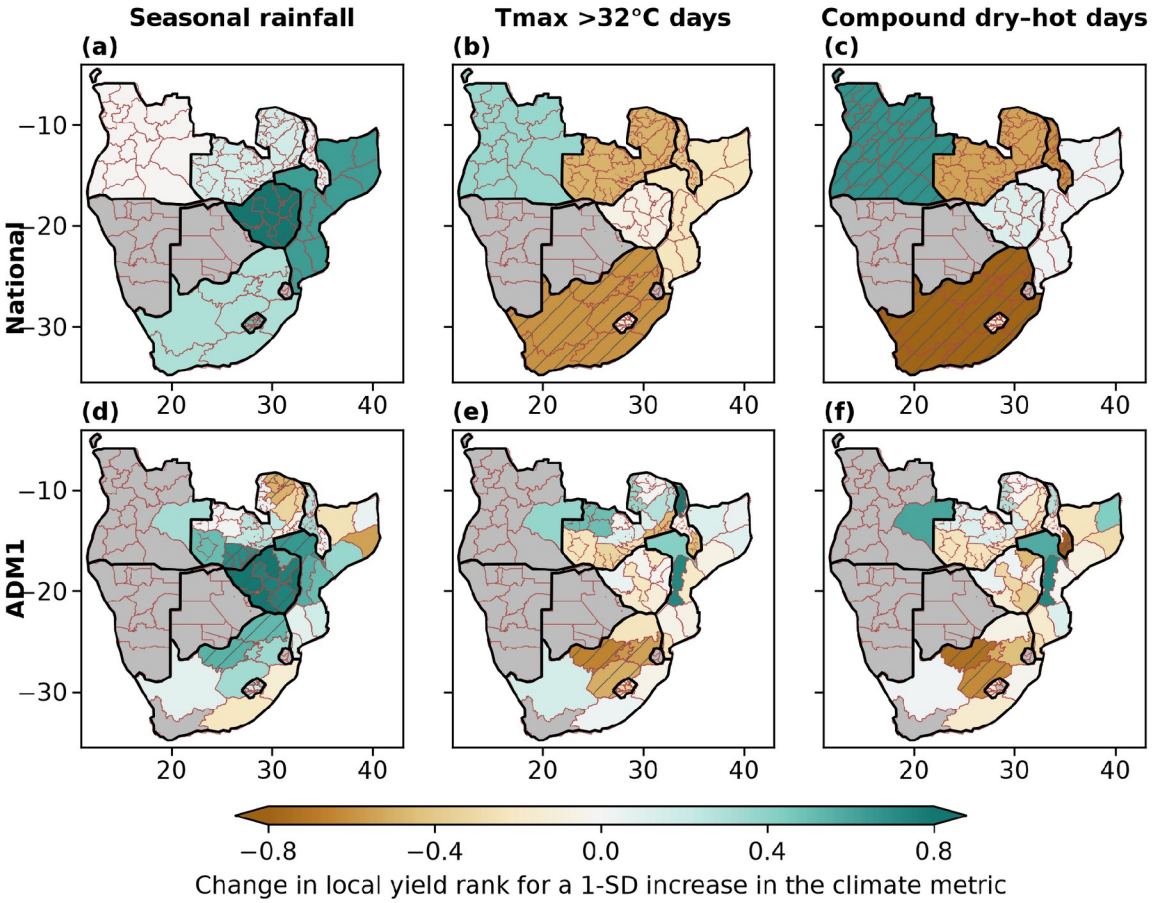


Figure S9. National and ADM1 climate–yield relationships. Columns show the change in yield rank per one-standard-deviation increase in seasonal rainfall, rainy-season days with Tmax >32°C and compound dry–hot days. The upper row uses national FAOSTAT maize-yield ranks, subset for each metric and country to years represented by at least one eligible HarvestStat ADM1 series. The lower row shows HarvestStat ADM1 maize-yield ranks. Climate variables in both rows are cosine-latitude-weighted averages over the fixed AHAD maize mask. Grey regions lack at least 15 paired yield–climate seasons (bottom row) or eligible HarvestStat data (top row). Hatching indicates that the pointwise 95% interval from 2,000 season bootstrap resamples excludes zero.

Robustness of climate–yield sensitivity estimates

We assessed the sensitivity of the climate–yield coefficients to temporal sampling, yield-window overlap and the choice of yield measure. First, we resampled individual seasons and consecutive blocks of three, five and seven seasons. The block resampling preserves some temporal structure and tests whether the coefficients depend disproportionately on particular periods. We also repeated the analysis after omitting each consecutive five-year period. These omission tests were conducted both by excluding the target-season observations only and by additionally excluding observations whose five-harvest yield-rank windows overlapped the omitted period. The resulting ranges describe sensitivity to the sampled period and are not confidence intervals.

We then compared the local five-harvest yield-rank measure with percentage yield anomalies calculated relative to a country-specific log-linear yield trend. The anomaly analysis was repeated with and without clipping the most extreme 1% of log residuals at each tail. For comparability, coefficients and intervals were expressed relative to the sample standard deviation of the corresponding yield measure over the common 40 complete seasons. Intervals were calculated from 2,000 five-year moving-block bootstrap samples. Across these tests, the sign and broad spatial pattern of the climate sensitivities were generally retained.

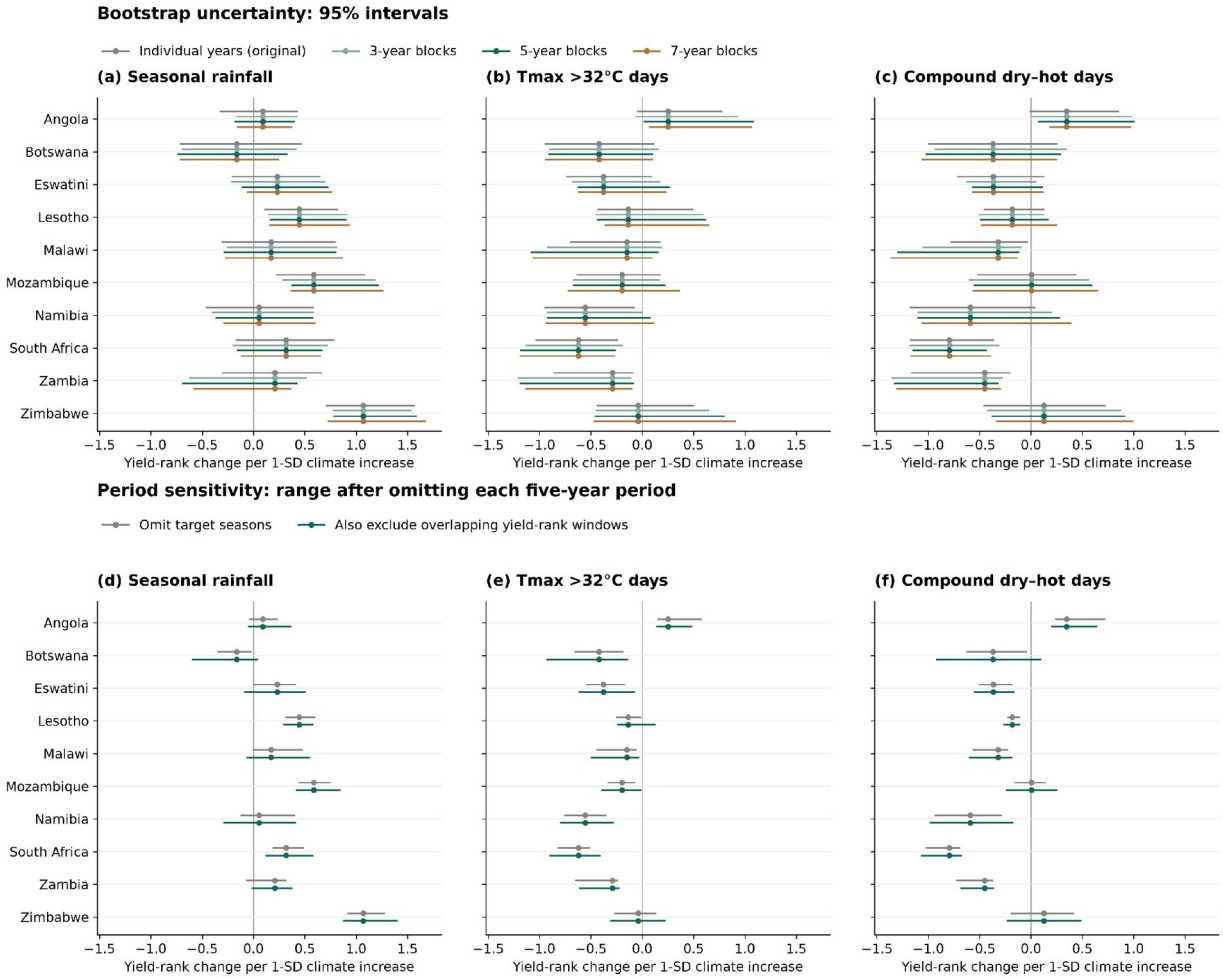


Figure S10. Sensitivity of climate–yield coefficients to temporal resampling and omitted periods. Columns show seasonal rainfall, rainy-season hot days and compound dry–hot days, using the country-specific regressions in Figure 1. Upper panels show the full-sample coefficients and 95% percentile intervals from 2,000 bootstrap samples using individual seasons or consecutive blocks of three, five or seven seasons. Lower panels show the full-sample coefficients and the ranges obtained after omitting each consecutive five-year period. The omission analysis either excludes the target-season observations alone or also excludes observations whose five-harvest yield-rank windows overlap the omitted period. Omission ranges are sensitivity ranges, not confidence intervals. Coefficients represent yield-rank change per country-specific 1991–2020 standard deviation of the climate metric.

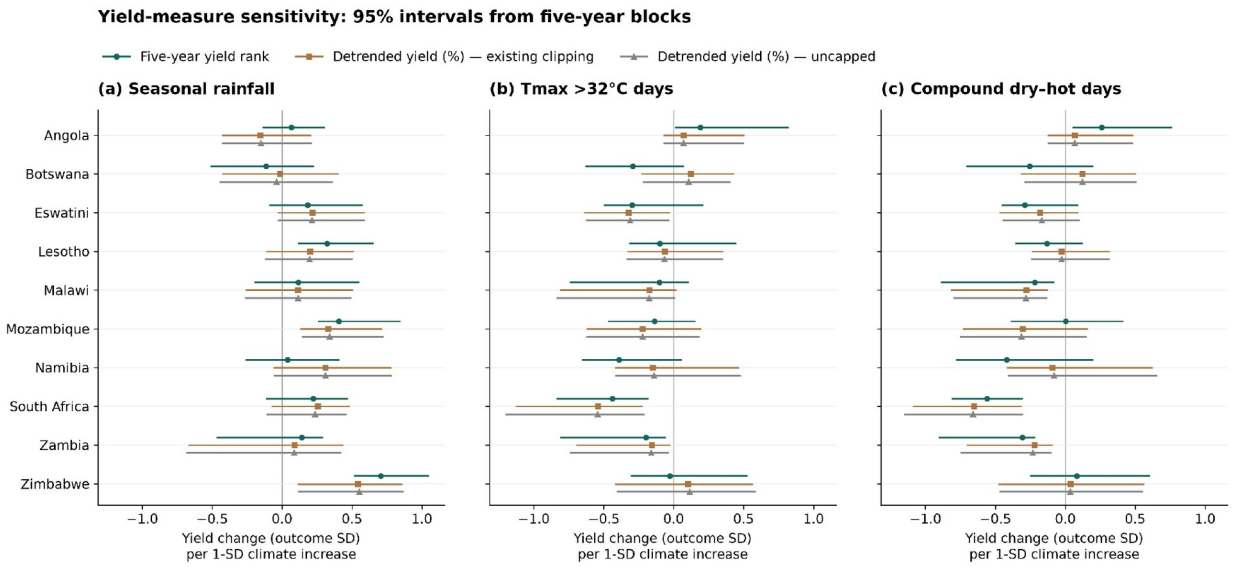


Figure S11. Sensitivity of climate–yield coefficients to the yield measure. Country-specific coefficients are shown for five-harvest yield ranks and percentage yield anomalies relative to a country-specific log-linear trend, with and without clipping log residuals at the 1st and 99th percentiles. Climate scaling and regression specifications are those used in Figure 1. Coefficients and intervals are divided by the sample standard deviation of the corresponding yield outcome across the 40 common complete seasons. Lines show 95% percentile intervals from 2,000 five-year moving-block bootstrap samples. These intervals describe sampling uncertainty and do not account for multiple spatial comparisons.

El Niño anomalies and yield decomposition

Regression-based decomposition of El Niño yield differences

Figure 3 and Figure S14 use a regression-based decomposition to estimate how much of the observed El Niño-associated yield difference is consistent with the historical sensitivity of maize yield to rainfall and heat. This is an attribution-style diagnostic rather than a causal regression in the strict econometric sense.

For each country, we constructed an annual panel for the 1983/84–2023/24 seasons containing the FAOSTAT maize-yield rank within a local five-harvest window, seasonal rainfall accumulated over the locally diagnosed rainy season, and the number of rainy-season days with maximum temperature above 32 °C. The local yield ranks reduce the influence of long-term changes in national yield levels. Climate variables were not temporally detrended or residualised.

Rainfall and hot-day counts were standardised separately for each country using the country-specific mean and sample standard deviation over 1991–2020. Thus, the standardised values represent departures from the local climatological distribution, and a one-unit change corresponds to one local standard deviation.

For each country, an ordinary least-squares model was fitted to all available seasons with complete data:

$$Y_t = \alpha + \beta_r R^*_t + \beta_h H^*_t + \varepsilon_t$$

where Y_t is the local yield rank, R^*_t is standardised seasonal rainfall and H^*_t is the standardised hot-day count. Because both predictors are included in the same model, β_r represents the rainfall association conditional on hot-day occurrence, while β_h represents the hot-day association conditional on rainfall. The joint regression allows rainfall and hot-day exposure to covary; it does not require the predictors to be independent. We assessed predictor dependence using country-specific Pearson correlations and variance inflation factors (VIF), which quantify the inflation of coefficient variance associated with correlated predictors. Rainfall–hot-day correlations ranged from −0.64 to 0.34, with VIF values of 1.02–1.71, indicating that multicollinearity was not severe.

The El Niño group comprised the moderate, strong and very strong seasons 1986/87, 1987/88, 1991/92, 1994/95, 1997/98, 2002/03, 2009/10, 2015/16 and 2023/24. These seasons were compared with all other seasons in the analysis period. For each country, the observed yield-rank difference was calculated as the mean yield rank in the El Niño seasons minus the mean yield rank in all other seasons.

The rainfall and heat contrasts were calculated in standard-deviation units as the corresponding El Niño-minus-other-season differences in R* and H*. The modelled rainfall contribution was calculated as $\beta_r \Delta R^*$, and the modelled hot-day contribution as $\beta_h \Delta H^*$. Their sum gives the combined modelled contribution. The unexplained remainder was defined as the observed yield-rank difference minus this combined contribution.

Uncertainty was estimated using 2,000 bootstrap repetitions. In each repetition, El Niño seasons were resampled with replacement within the nine-season El Niño group, while non-El Niño seasons were independently resampled with replacement from the reference pool. The

regression coefficients, climate contrasts and all resulting contributions were recalculated for every bootstrap sample. The reported intervals are the 2.5th and 97.5th percentiles of these bootstrap distributions. A contribution was considered robust when its interval excluded zero.

The decomposition therefore asks how much of the observed El Niño yield difference would be expected from the estimated country-specific rainfall and hot-day relationships, given the climate anomalies experienced during El Niño. The residual includes effects of other climate variables, nonlinearities, interactions, non-climatic influences and sampling uncertainty; it should not be interpreted as a purely causal effect of unmeasured climate processes.

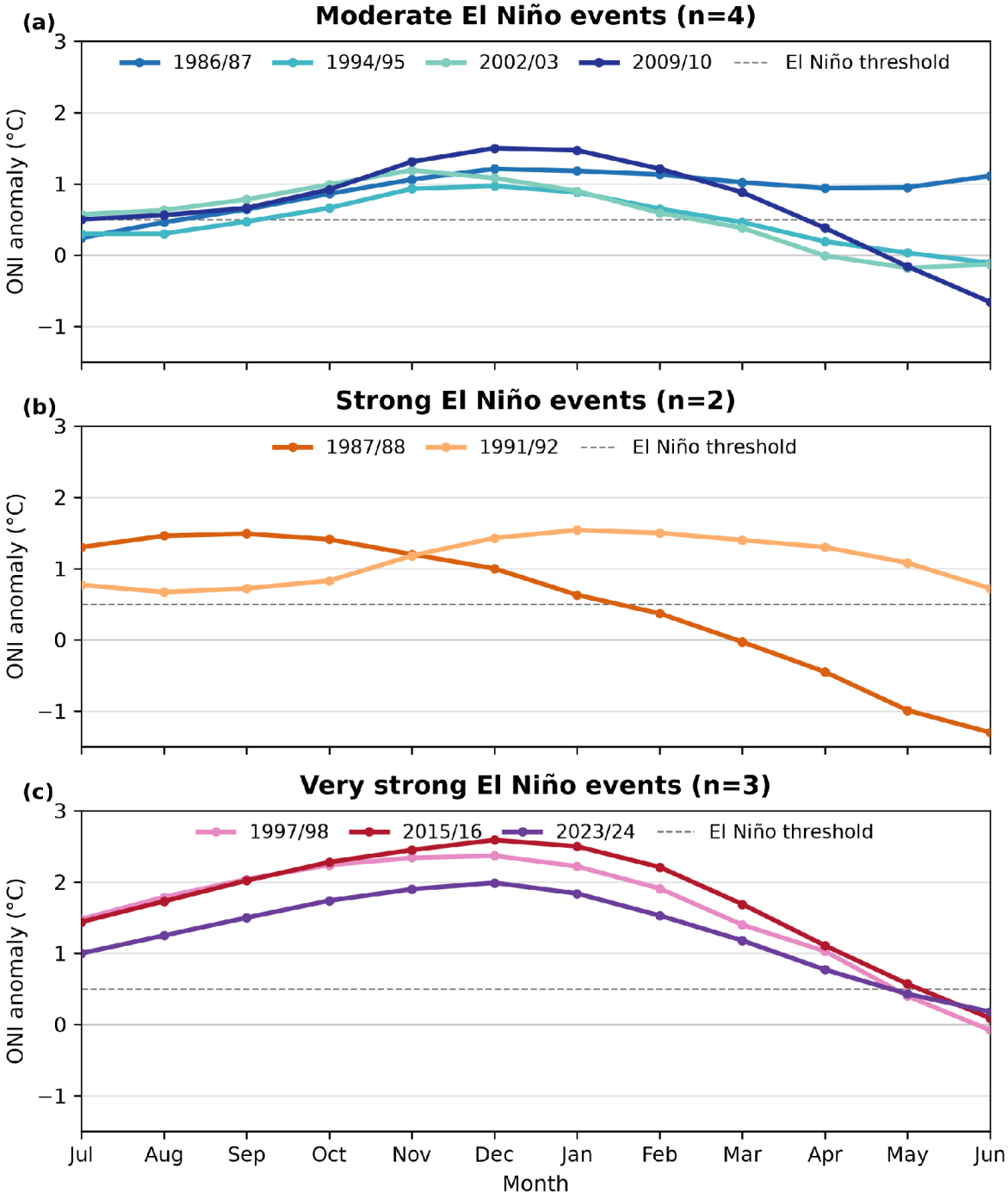


Figure S12. Evolution of the CPC Oceanic Niño Index (ONI) during the El Niño events used in this study. Panels show mutually exclusive (a) moderate, (b) strong and (c) very strong event groups from July of the development year to June of the following year. ONI is the centred three-month running Niño3.4 sea-surface-temperature anomaly.

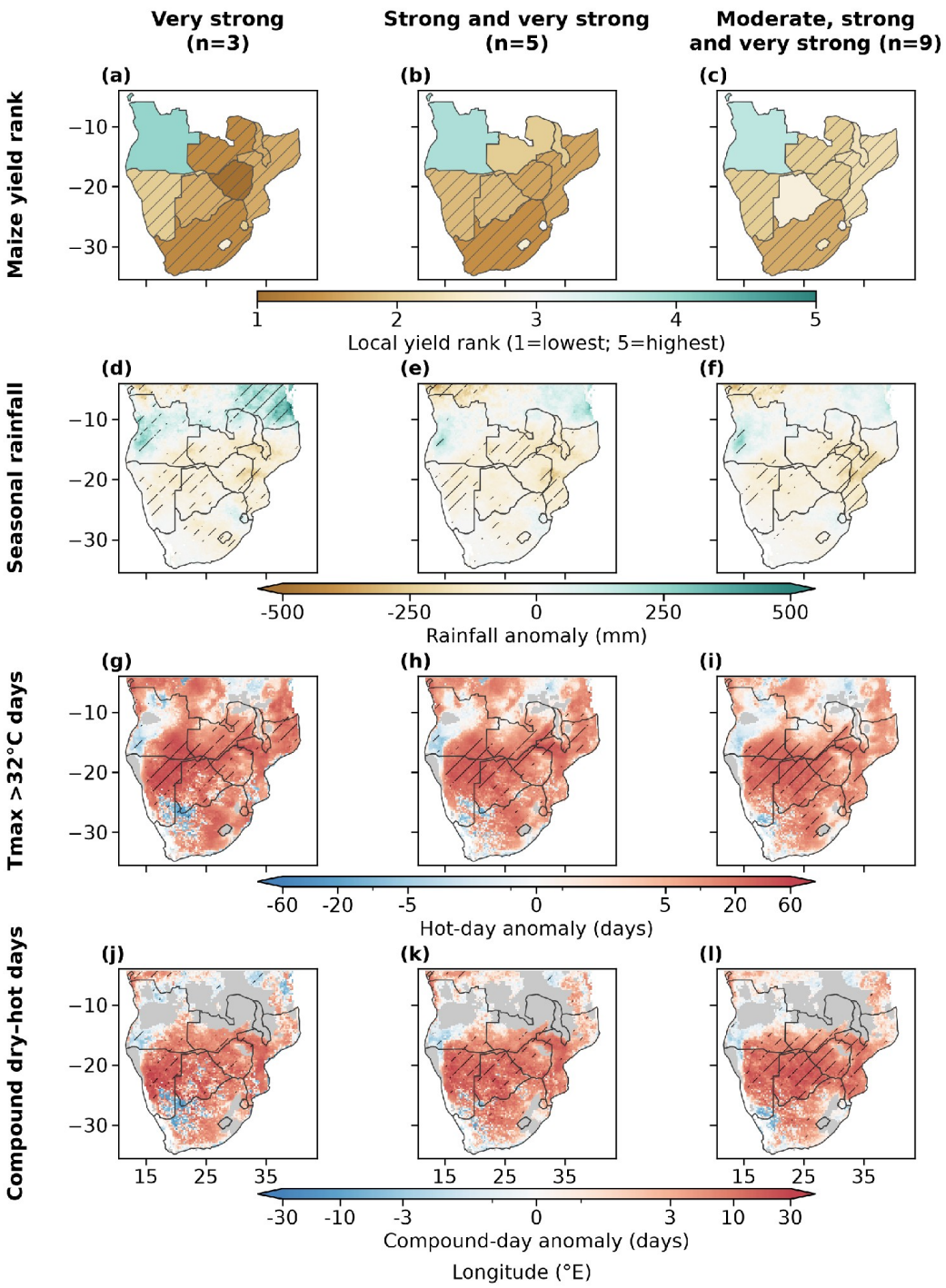


Figure S13. Local maize-yield ranks and rainy-season climate anomalies for El Niño event groups. Columns show very strong; strong and very strong; and moderate, strong and very strong events. Rows show: mean maize yield rank, seasonal rainfall, occurrence of Tmax >32°C days, and occurrence of compound hot days preceded by at least five consecutive days with rainfall <1 mm/day. Climate anomalies are relative to seasons outside the respective event group over 1983/84–2023/24. Hatching denotes pointwise 95% percentile-bootstrap intervals excluding zero for the selected-event-minus-other-season difference, based on 2,000 resamples within each group. Grey indicates fewer than one day per season across the analysis period for either the control or El Niño group.

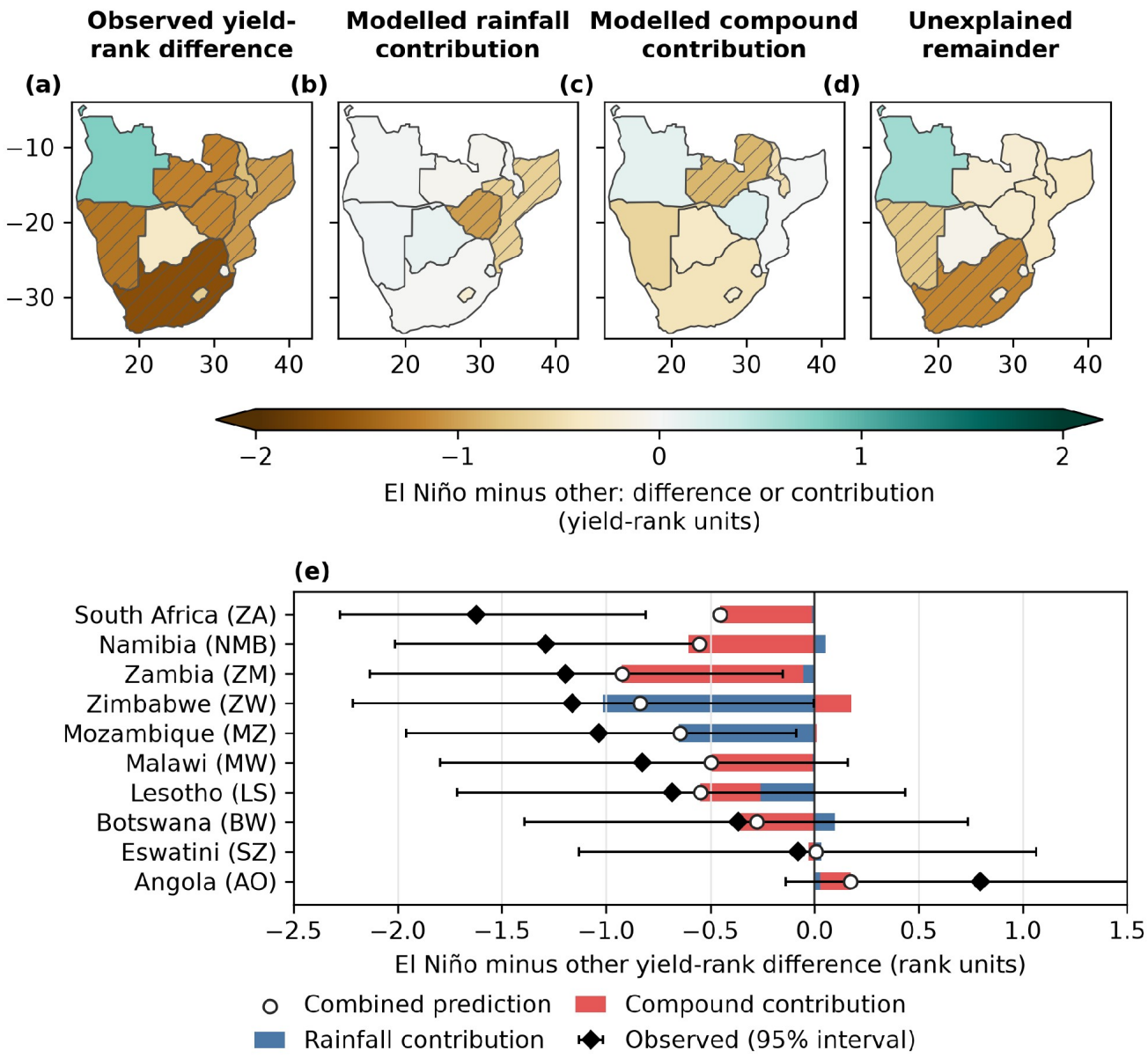


Figure S14. As for Figure 3 but using compound dry–hot-day counts rather than hot days.

Robustness of the yield decomposition

We also assessed sensitivity of the decompositions in Figure 3 and Figure S14 to temporal dependence and individual El Niño episodes (Figures S15–S19). The national panel comprises 40 complete seasons during 1983/84–2023/24, including nine El Niño seasons; 1984/85 lacks CPC temperature. Other complete seasons form the reference group. For each model, 5,000 replicates resampled seasons independently within each group, or circular blocks of three, five or seven calendar years from the 41-season grid, retaining the missing year. Each replicate refitted regression coefficients and group climate contrasts, holding local five-harvest yield ranks and climate scaling fixed.

The 2.5th–97.5th percentile intervals are conditional on these data and models. Replicates required at least three distinct El Niño seasons, ten reference observations and a nonsingular fit; intervals required at least 95% valid replicates. The small event sample and assumed block structure limit accuracy. Intervals are pointwise, without multiple-comparison correction, and exclude some uncertainty in yield measurement, rank construction and model form.

We also refitted models after omitting individual El Niño seasons or entire episodes, grouping 1986/87 and 1987/88. A further check removed rows whose five-harvest rank windows overlapped an omitted season's window. Omitted events were removed, not reassigned to the reference group. Figures S18 and S19 show episode-omission changes; these are sensitivity ranges, not confidence intervals.

For the rainfall–hot-day model, the three-, five- and seven-year block intervals remain below zero for the heat contribution in South Africa, Namibia and Zambia, and for the rainfall contribution in Zimbabwe and Mozambique (Figure S15). South Africa's residual is −1.04 yield-rank units, with a five-year block interval of −1.59 to −0.13. Its residual remains negative after every episode omission (−1.22 to −0.72) and when overlapping rank windows are also excluded (−1.22 to −0.56). In the compound-day formulation, the residual intervals remain below zero in South Africa and Namibia for all three block lengths (Figure S16). These residuals remain model-dependent associations and do not identify a non-climatic mechanism.

We compared the estimated heat and rainfall contributions directly by subtracting rainfall from heat within each bootstrap replicate (Figure S17). The five-year block interval for this contrast includes zero in every country for the hot-day model. Thus, the estimated ordering of contributions is not equivalent to a well-established difference between them. In the compound-day model, Zambia's compound contribution is more adverse than its rainfall contribution under this interval criterion.

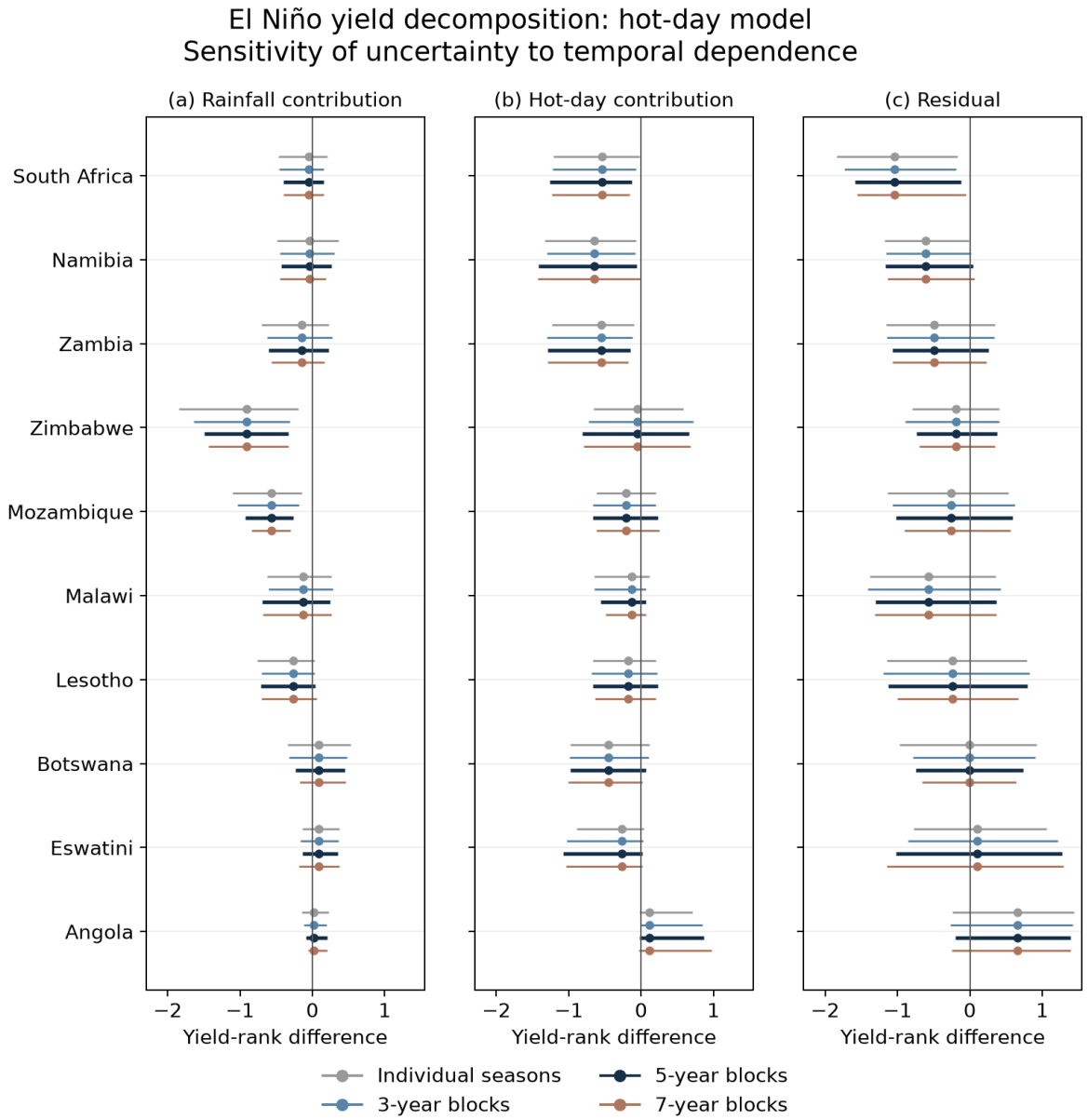


Figure S15. Sensitivity of the rainfall–hot-day yield decomposition to temporal resampling. Points show the original rainfall contribution, hot-day contribution and residual; intervals show the 2.5th–97.5th percentiles of 5,000 replicates using individual seasons or circular three-, five- and seven-year blocks. Regression coefficients and group climate contrasts are refitted in each replicate. Negative values indicate lower yield ranks during El Niño. Intervals are approximate and pointwise; local yield ranks and climate scaling remain fixed.

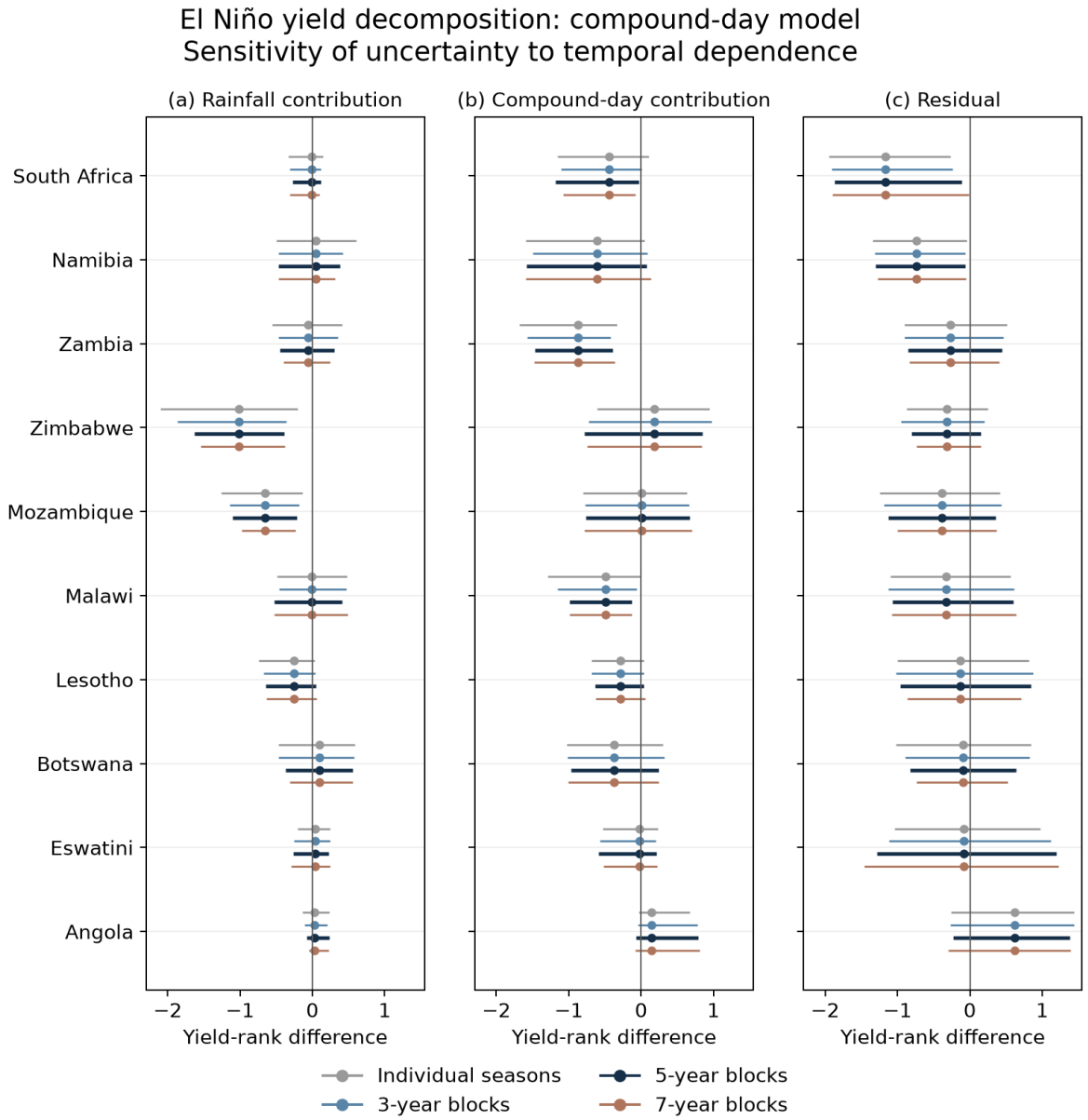


Figure S16. As Figure S15, replacing hot-day exposure with compound dry–hot-day exposure. The rainfall, compound-day and residual estimates use the original model formulation; only temporal sampling and its associated uncertainty are reassessed.

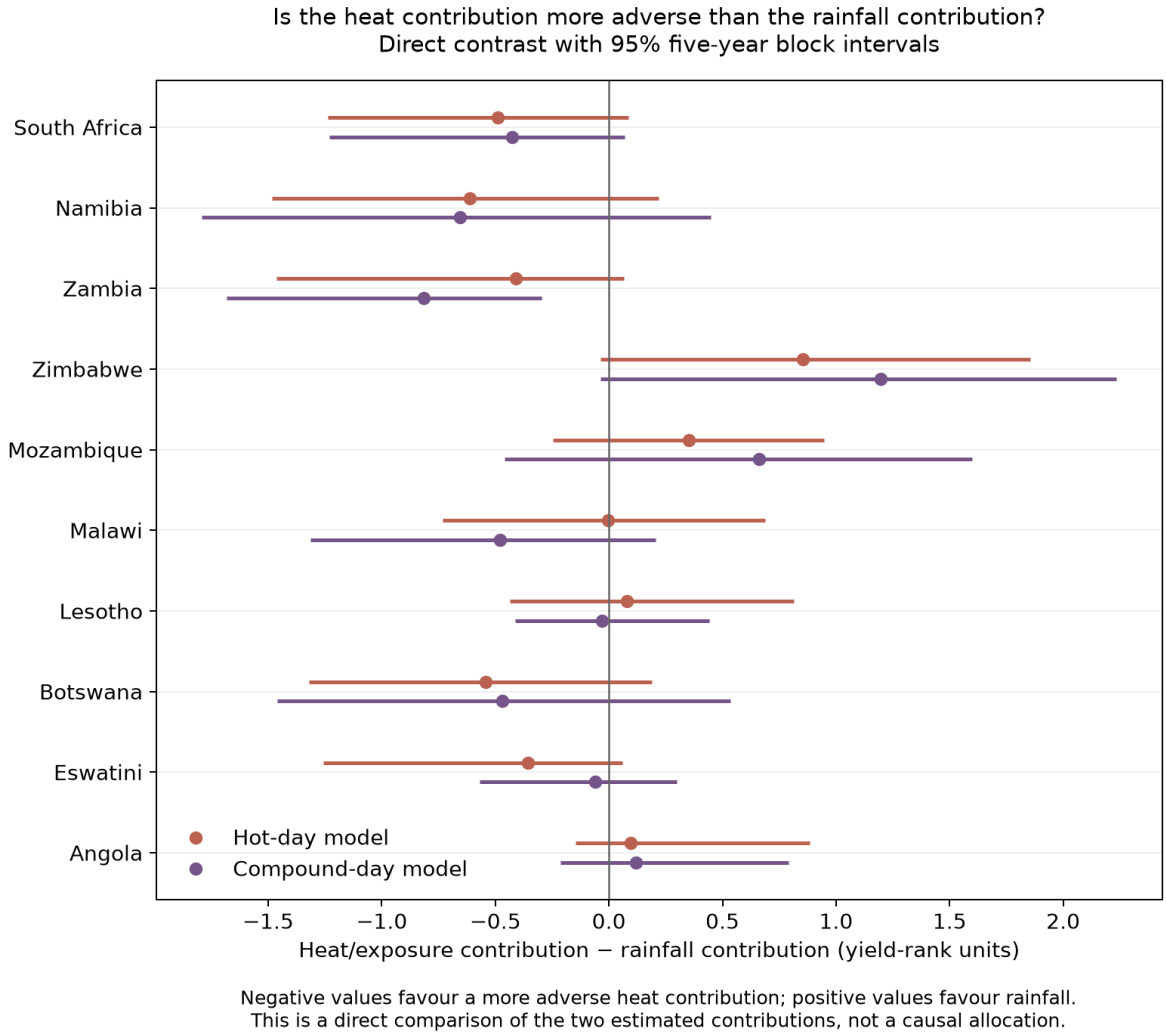


Figure S17. Direct comparison of the heat/exposure and rainfall contributions to El Niño-associated yield differences. Points show heat/exposure minus rainfall for the hot-day and compound-day formulations; bars show paired 95% percentile intervals from 5,000 five-year block resamples. Negative values indicate a more adverse heat/exposure contribution. An interval spanning zero does not establish which contribution is larger. These are conditional, pointwise comparisons rather than causal allocations.

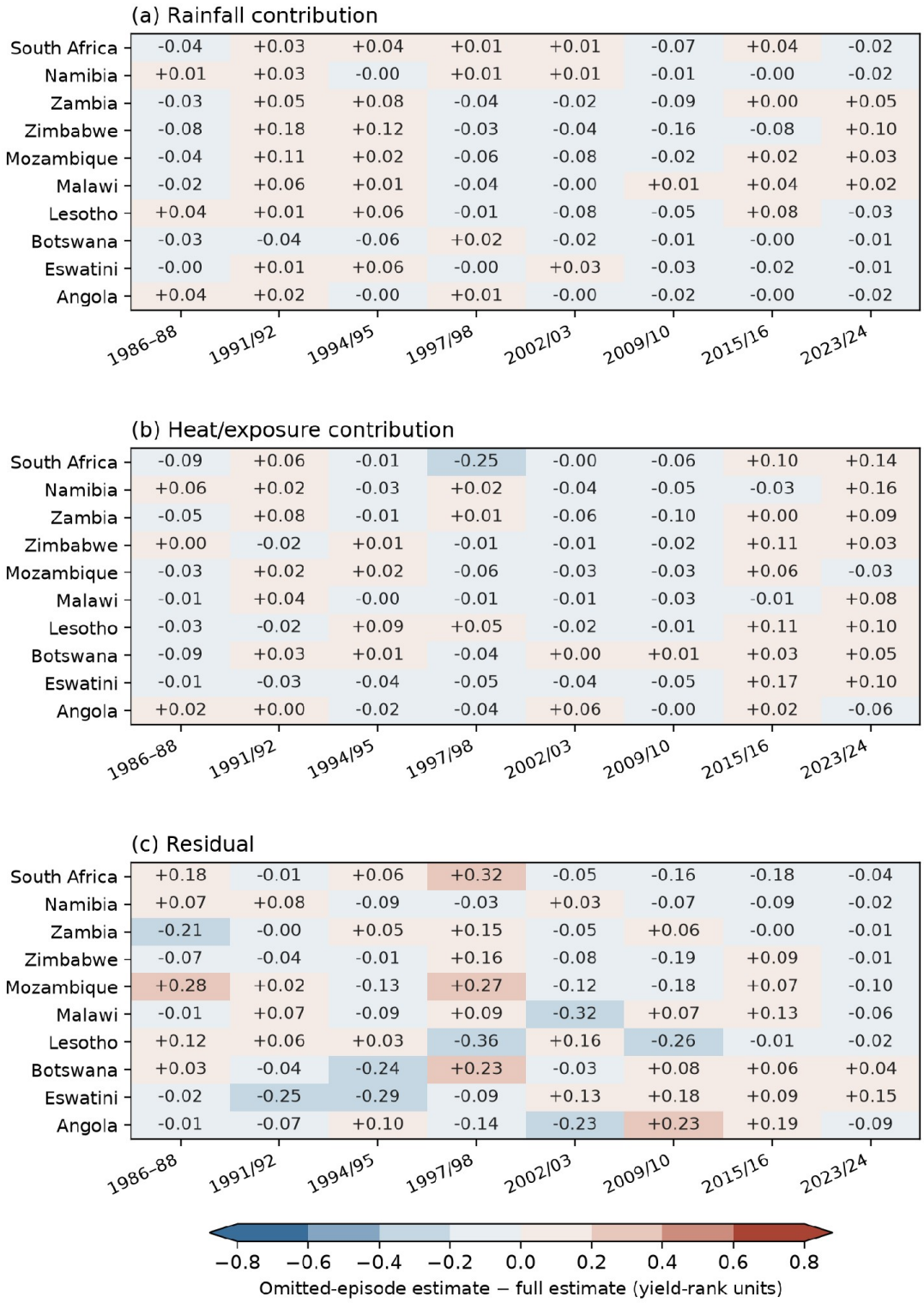


Figure S18. Sensitivity of the rainfall–hot-day decomposition to omitting each El Niño episode. Values are the estimate after omission minus the full-sample estimate, in yield-rank units, for rainfall, heat and the residual. Both coefficients and group contrasts are refitted. The consecutive 1986/87 and 1987/88 seasons are omitted together. Positive values indicate a shift towards a less adverse contribution or residual. This is an influence diagnostic, not a confidence interval.

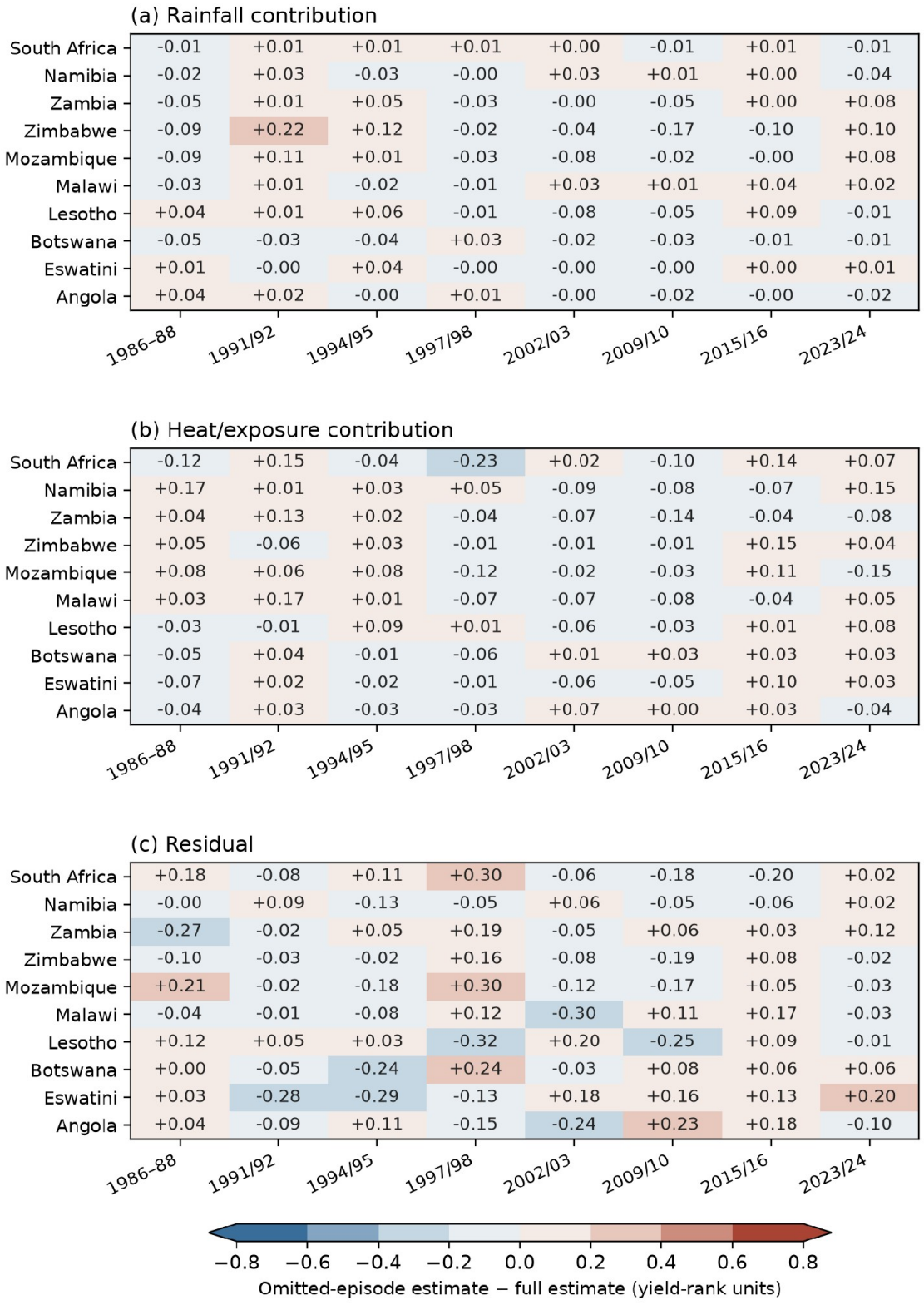


Figure S19. As Figure S18, for the rainfall–compound-day formulation. All other modelling and omission choices are unchanged.

Sensitivity to additional climate metrics

For the sensitivity analysis in Figure S20, the five additions were assessed separately on identical spatial and temporal support: 40 seasons from 1983/84 to 2023/24, excluding 1984/85 because CPC temperature was unavailable, including nine El Niño seasons. Within-season timing adds early-minus-middle and late-minus-middle contrasts for both rainfall and hot-day totals over locally diagnosed rainy-season thirds; these thirds do not identify actual crop stages. Country-year averages use common valid maize-growing grid cells and require at least two-thirds area coverage. Prediction skill uses observed climate, with each consecutive five-calendar-year block excluded in turn and training observations removed wherever their underlying five-harvest rank windows overlap those of the test observations. ACC is calculated from the pooled paired predictions and observations, separately centred without further detrending. Residual-change intervals refit models using 2,000 paired circular five-calendar-year moving-block bootstrap samples. ACC-change intervals use the same block resampling of fixed observation and prediction triples and therefore describe score uncertainty conditional on the fitted validation models. Intervals are pointwise, without a multiple-testing correction. The rainfall–heat interaction is retained as a separate exploratory model-form check, outside the five additions shown in Figure S20.

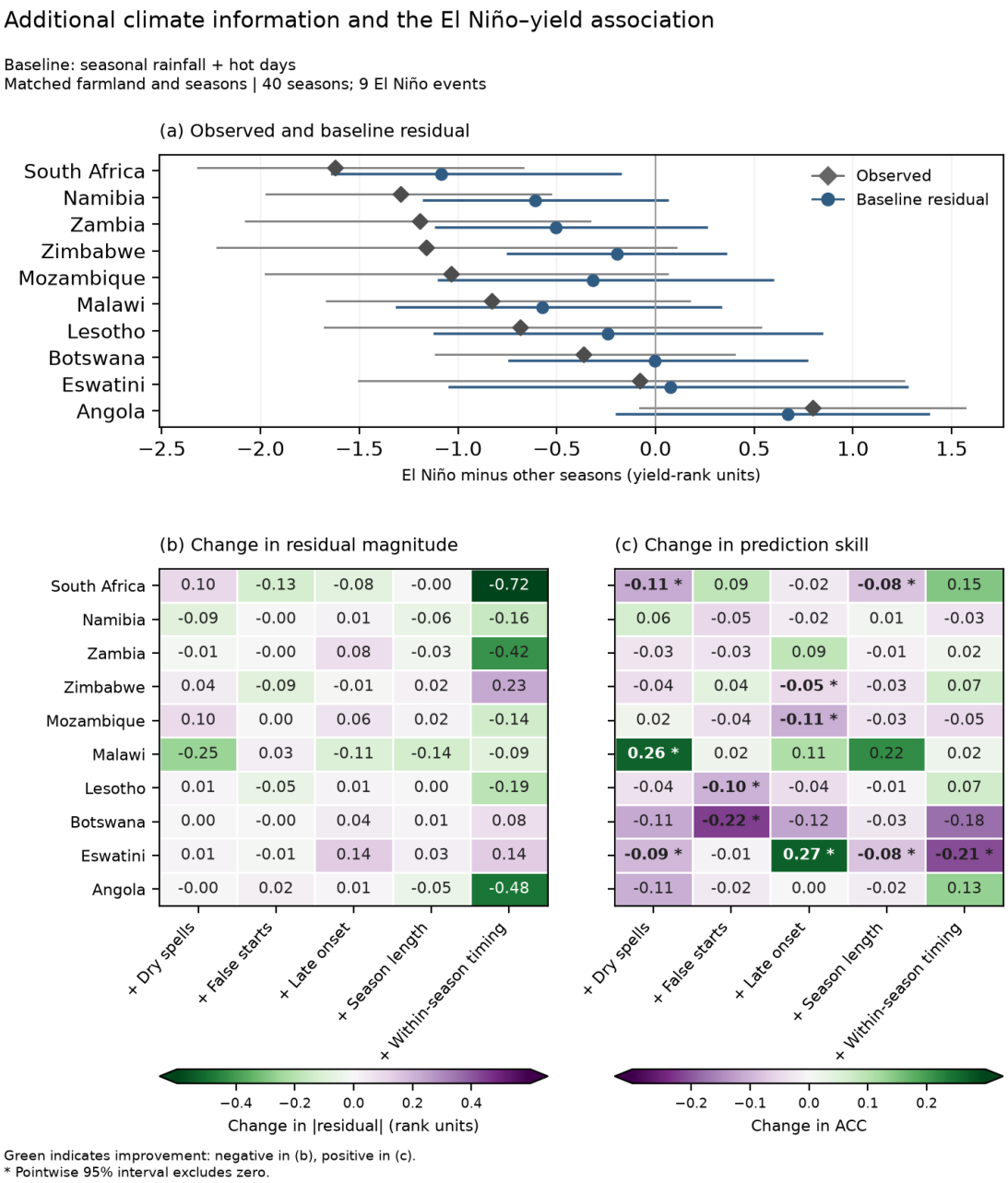


Figure S20. Sensitivity of the El Niño–maize yield association to five additions to a seasonal rainfall–hot-day model. All comparisons use matched maize-growing cells and 40 seasons, including nine El Niño seasons. (a) Observed and baseline residual El Niño-minus-other-season yield-rank differences, with 95% intervals. (b) Change in residual magnitude: absolute extended-model residual difference minus absolute baseline residual difference, in rank units. (c) Change in prediction skill: extended-model ACC minus baseline ACC, in correlation units. ACC is the Pearson correlation of separately centred observed and predicted ranks, pooled across five-year leave-one-block-out predictions; training ranks with harvest windows overlapping test rank windows are excluded. Prediction uses observed climate, not meteorological forecasts. Green indicates improvement: negative in (b), positive in (c). Intervals use 2,000 paired five-calendar-year moving-block bootstrap samples; ACC intervals resample fixed observation/prediction triples without refitting validation models. Asterisks mark pointwise 95% intervals excluding zero, without multiple-testing correction. Within-season timing uses rainfall and hot-day contrasts among local rainy-season thirds, not observed crop stages. See Supplementary Methods for details.

Sensitivity to rainfall–heat interaction

We added a product of seasonal rainfall and heat exposure to each additive model, retaining both main effects. Exposure was represented by hot-day counts or compound dry–hot-day counts. Comparisons used the same matched cells, 40 seasons (including nine El Niño seasons), cross-validation and block-resampling procedures as the additional-metric analysis in Figure S20.

Adding the interaction did not produce a statistically robust reduction in the magnitude of the residual El Niño association in any country for either formulation (Table S3). Prediction skill improved in Botswana for both formulations and declined in Angola for the hot-day model; other changes in ACC had intervals spanning zero. This specific interaction therefore provides no clear explanation for the residual association, while leaving other nonlinear responses possible.

Table S3. Changes in residual magnitude and cross-validated prediction skill after adding a rainfall-by-exposure interaction. Values are estimates with pointwise 95% intervals in brackets.

Country	Hot-day model Change in residual magnitude	Hot-day model Change in prediction skill	Compound-day model Change in residual magnitude	Compound-day model Change in prediction skill
South Africa	−0.03 [−0.21, 0.27]	−0.01 [−0.09, 0.07]	0.00 [−0.11, 0.22]	−0.04 [−0.12, 0.01]
Namibia	−0.02 [−0.28, 0.13]	0.02 [−0.03, 0.07]	−0.01 [−0.19, 0.07]	−0.03 [−0.08, 0.01]
Zambia	−0.14 [−0.65, 0.14]	0.01 [−0.05, 0.18]	−0.03 [−0.41, 0.17]	−0.11 [−0.46, 0.01]
Zimbabwe	−0.12 [−0.24, 0.23]	−0.05 [−0.15, 0.03]	−0.05 [−0.20, 0.13]	−0.07 [−0.20, 0.04]
Mozambique	0.07 [−0.24, 0.28]	−0.05 [−0.12, 0.01]	−0.03 [−0.17, 0.11]	−0.02 [−0.05, 0.00]
Malawi	−0.13 [−0.37, 0.24]	0.03 [−0.11, 0.16]	−0.04 [−0.32, 0.25]	−0.01 [−0.15, 0.06]
Lesotho	−0.06 [−0.28, 0.23]	−0.06 [−0.27, 0.18]	−0.08 [−0.27, 0.22]	−0.02 [−0.12, 0.08]
Botswana	0.10 [−0.33, 0.24]	0.24 [0.03, 0.47]	0.06 [−0.33, 0.23]	0.28 [0.03, 0.60]
Eswatini	0.11 [−0.27, 0.28]	0.14 [−0.17, 0.44]	−0.08 [−0.29, 0.30]	0.10 [−0.06, 0.27]
Angola	0.00 [−0.29, 0.12]	−0.26 [−0.45, −0.06]	−0.02 [−0.26, 0.14]	0.02 [−0.11, 0.16]

Negative change in residual magnitude indicates a smaller absolute El Niño-minus-other-season residual difference (yield-rank units). Positive change in prediction skill indicates higher ACC (correlation units). Prediction uses observed climate and five-year leave-one-block-out validation, excluding overlapping yield-rank windows. Intervals use 2,000 paired circular five-year block resamples: residual-change models are refitted, whereas ACC intervals resample fixed predictions and are conditional on those fits. No multiple-testing correction is applied. The matched-support baselines may differ slightly from Figures 3 and S14.

Sensitivity to the choice of reference seasons

We repeated the climate-anomaly and yield-decomposition comparisons using neutral seasons as the reference (Figures S21 and S22). The original nine moderate, strong and very strong El Niño seasons were retained. Neutral seasons were defined by October–December ONI strictly between −0.5°C and +0.5°C, after rounding the archived index to one decimal place. This selected ten seasons: 1985/86, 1989/90, 1990/91, 1992/93, 1993/94, 1996/97, 2001/02, 2003/04, 2012/13 and 2013/14.

For Figure S21, climate anomalies were recalculated relative to the neutral-season mean. Absolute local yield ranks were unchanged; composite hatching tests El Niño-minus-neutral differences in both yield and climate. Uncertainty uses 2,000 whole-season bootstrap resamples drawn separately within the El Niño and neutral groups, with common sampled years across grid cells and variables. Individual-event panels remain descriptive.

For Figure S22, the regression remained fitted to all 40 complete seasons, retaining the original yield ranks and 1991–2020 climate standardisation. Only the reference group used to calculate the yield and climate contrasts changed. Uncertainty uses 2,000 paired whole-season bootstrap resamples drawn separately within three strata: the nine El Niño seasons, ten neutral seasons and 21 remaining seasons. All three strata enter each regression refit, and the El Niño-minus-neutral climate and yield contrasts are recalculated in each repetition. Both figures show pointwise 95% percentile intervals, without temporal-block or multiple-testing adjustment.

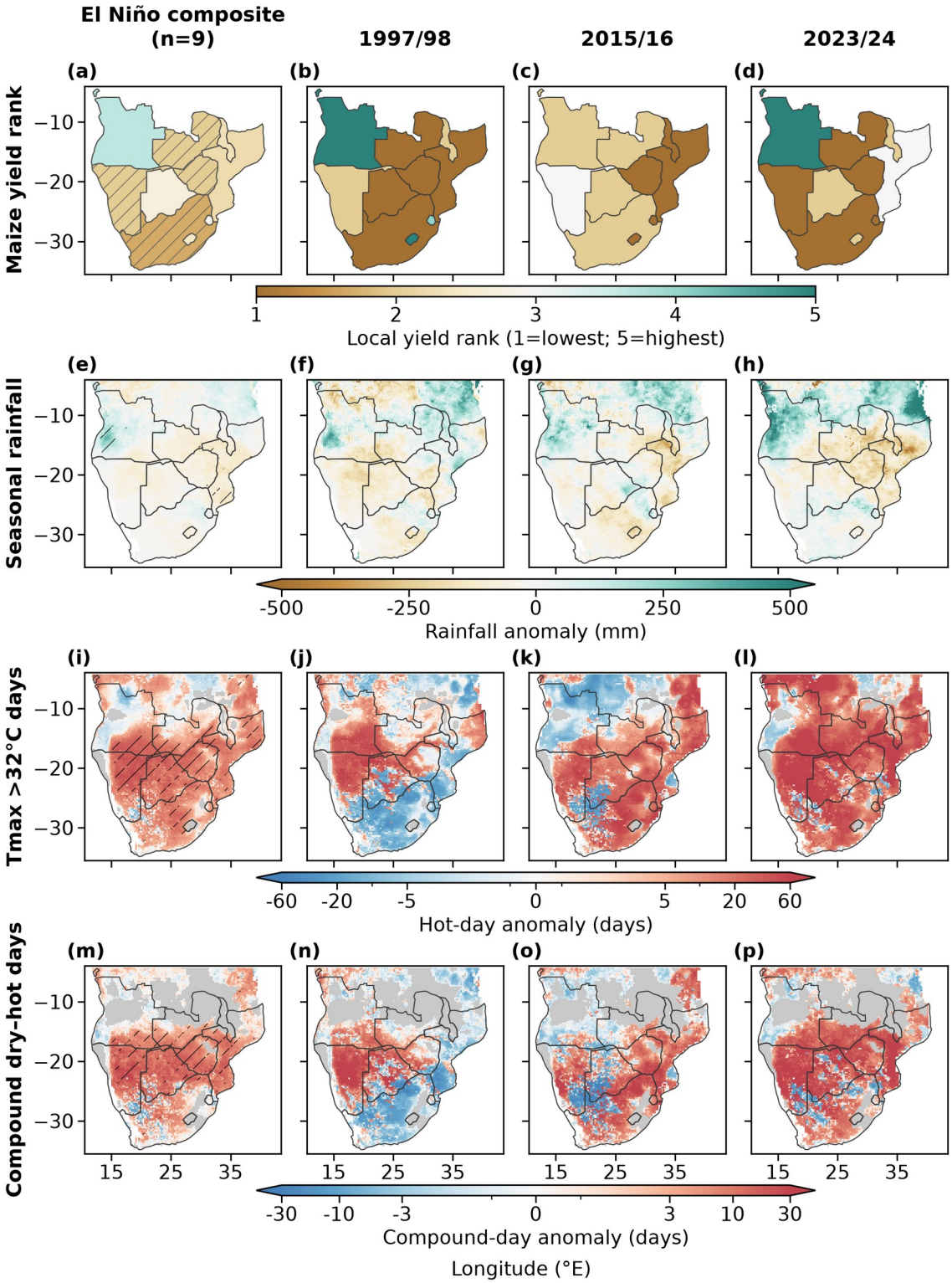


Figure S21. As Figure 2, with climate anomalies calculated relative to the ten neutral seasons defined above. Yield colours show the same local five-harvest ranks as Figure 2. Hatching in the composite column denotes El Niño-minus-neutral differences whose pointwise 95% percentile-bootstrap intervals exclude zero, based on 2,000 separate-group whole-season resamples; it has been recalculated for both yield and climate. Individual-event panels have no inference markings. Colours, scales and full-record rare-event masking are unchanged.

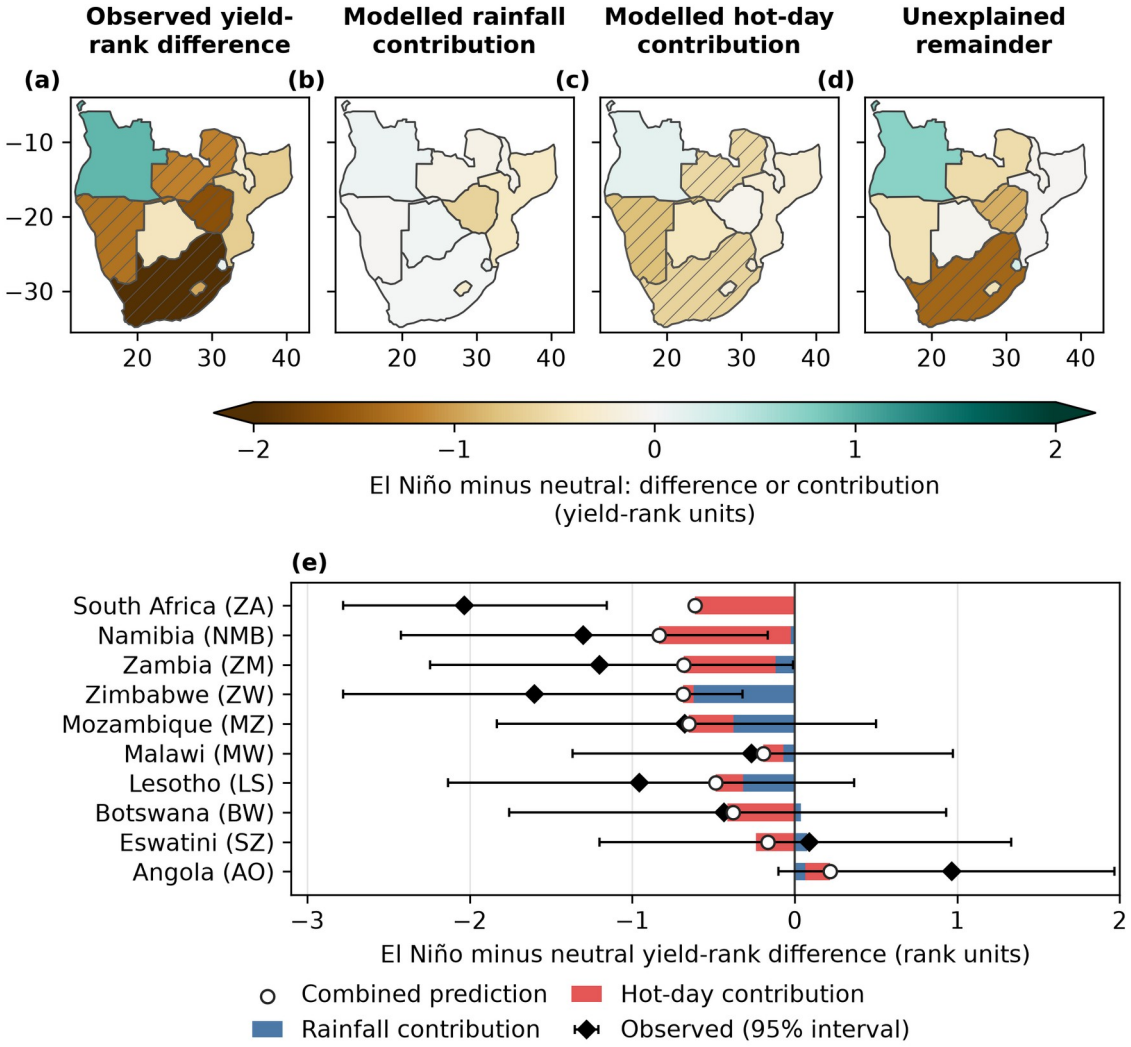


Figure S22. As Figure 3, comparing the nine El Niño seasons with ten neutral seasons while retaining the all-season rainfall–hot-day regression. Maps show the observed yield-rank difference, estimated rainfall and hot-day contributions, and residual. Hatching denotes pointwise 95% intervals excluding zero. In panel (e), bars show the rainfall and hot-day contributions, open circles their sum, and diamonds the observed difference with its 95% interval. Intervals use 2,000 paired whole-season resamples within El Niño, neutral and remaining-season strata, with all strata retained in each regression refit. The horizontal axis is extended to include the South African interval.

Sensitivity to the heat-exposure window

We repeated the rainfall–heat decomposition using (i) the percentage of valid days with Tmax >32°C within the annually diagnosed rainy season, including the existing climatological fallback, and (ii) hot-day counts within each grid cell's fixed climatological onset–cessation window. Percentages were calculated per grid cell before country averaging. All variants retained annual-season rainfall and the original yield ranks, and used the same valid maize-growing cells and 40 complete seasons. Windows required at least 98% paired rainfall–temperature daily coverage; country averages required at least two-thirds of maize-mask area. The two-group, 2,000-resample annual bootstrap used identical draws across variants, with coefficients and El Niño contrasts recalculated in each sample. Intervals for changes were calculated from paired differences, including differences in absolute residual magnitude.

The diagnosed rainy season approximates the growing season, limiting exposure counts to the period when crops are assumed to be present. Fixed windows are a sensitivity check rather than a corrected crop calendar: they may include hot days before planting or after harvest. Median absolute changes in estimated heat contributions were 0.03 yield-rank units for percentage exposure and 0.04 for fixed-window counts; maximum changes were 0.10 and 0.20 units, respectively. Neither alternative robustly reduced residual magnitude in any country. The largest fixed-window change occurred in Zambia, where the estimated heat contribution became smaller and its interval included zero.

Forecast processing and verification

Analogue downscaling methodology

The downscaling approach uses a historical analogue method to translate coarse-resolution NeuralGCM and ECMWF rainfall forecasts onto a 0.25° degraded TAMSAT grid. For each 30-day forecast window, the hindcast rainfall is first interpolated to the 0.25° grid and the total rainfall is calculated separately for each ensemble member. At each grid cell, this forecast total is compared with 30-day rainfall totals drawn from the historical TAMSAT record. The closest historical windows are then used to estimate the local probability of the meteorological metric under consideration.

The analogue translation is applied separately to each ensemble member. For each member, the event probability is estimated as the proportion of its 40 closest historical analogue windows, in which the event occurred (sampled from the 1983–2025 TAMSAT record). These member-level probabilities are then averaged across the ensemble to produce the final downscaled forecast probability. This approach preserves both the spread among ensemble members and the range of local outcomes observed historically under similar rainfall conditions.

Several methodological choices were tested before fixing the final configuration. The selected method uses 40 analogues, with equal weighting rather than distance weighting. Candidate analogues are restricted to a ±15-day seasonal window around the target date, allowing a larger and more stable analogue pool than a strict calendar-month selection while retaining seasonal relevance. Analogue similarity is measured using the difference in log-transformed rainfall totals, which performed slightly better overall than matching absolute totals and was more robust for the wet-event metrics. Percentile-based matching was tested but did not improve performance and was therefore not retained.

Forecast-observation pairing and verification

Forecasts were paired with observations according to the target period rather than the forecast initialisation date. We evaluate 30-day target periods beginning on 1 November and 1 March. The 0-day lead uses forecasts initialised at the beginning of the target month, while the 30-day lead uses forecasts initialised one month earlier. Forecast metrics were calculated from the corresponding 30-day forecast windows and compared with the matching observed TAMSAT and CPC fields.

For each grid cell, observed tercile thresholds were calculated from the available verification-period observations. ROC-AUC was then calculated for lower-tercile accumulated-rainfall events and upper-tercile mean-Tmax and compound dry–hot-day events. Compound events were defined consistently with the historical analysis: a compound day had Tmax >32 °C immediately preceded by at least five consecutive days with rainfall below 1 mm day^{-1}. ROC-AUC measures the ability of the forecast to discriminate event from non-event years and does not assess probability calibration.

ACC was calculated as the Pearson correlation between forecast and observed anomalies across the paired years. Anomalies were calculated relative to the corresponding climatological mean, with the same reference period applied to forecasts and observations. Comparisons between lead times or forecast systems used the same matched years wherever possible; grid cells with

insufficient valid paired observations or with no variability in either the forecast or observed series were excluded. Neither forecast nor observed time series were detrended, consistent with the main-text skill assessment.

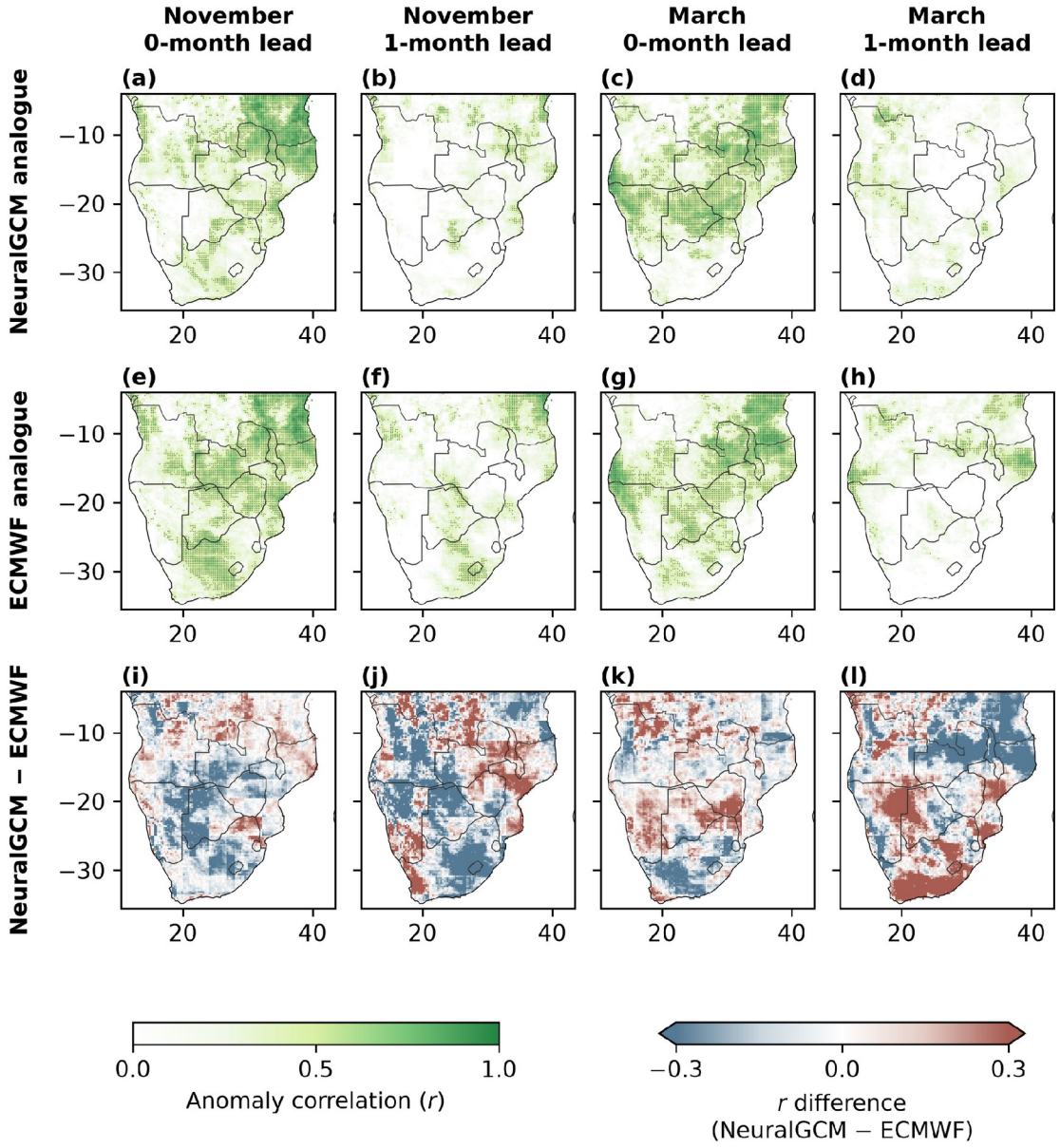


Figure S23. As for Figure 5 but using ACC (Anomaly Correlation Coefficient: the Pearson correlation of separately centred forecast and observed totals on identical paired years, with trends retained)

Sensitivity of the El Niño forecast-skill comparison

The forecast comparison in Figure 6 subtracts the arithmetic mean ACC from 10,000 equally sized control subsamples from ACC across the selected El Niño seasons. Each subsample is drawn without replacement from the available neutral and La Niña pool and contains eight or nine seasons, matching the El Niño sample for that panel. Dots mark El Niño ACC outside the pointwise central 95% of control correlations. This envelope describes the distribution of matched-size control correlations, with El Niño ACC held fixed; it is not a confidence interval for the underlying difference between the regimes.

The analysis uses raw ECMWF and observational pairs for the 42 calendar seasons 1983/84–2024/25. There are nine selected El Niño seasons, with eight for November Tmax because the 1986 observed window is incomplete. The control pool contains 28 neutral and La Niña seasons with October–December ONI below 0.5°C; other warm seasons are excluded. Forecast–observation availability is matched across leads. Verification windows are 1–30 November and 1–30 March, using same-month and preceding-month initialisation. Cells are displayed only where the El Niño correlation is finite and at least 95% of the control draws yield a finite correlation.

We assessed sensitivity to individual El Niño episodes by omitting each episode in turn (Figure S27). For this check, the comparison is El Niño ACC minus ACC across all available control seasons, rather than the mean of matched-size control correlations used in Figure 6. The control pool remains fixed, and 1986/87 and 1987/88 are removed together. Dots identify cells where all omission correlations are defined and the sign of the full-sample difference is retained after every omission. This is a leave-one-episode-out influence check, not a significance test or an estimate of confidence-interval coverage. Grid-cell trends and the original assessment domain are retained.

For March rainfall with previous-month initialisation, the full-control comparison gives a mean ACC difference of 0.077 over maize cells. The difference is positive over 62.9% of maize-mask area, while its sign remains positive after every episode omission over 28.4% of the area. These summaries use cosine-latitude weights over the fixed maize mask in the ten study countries and average grid-cell correlations, rather than correlating country-mean series. The fractions describe spatial coverage, not regional significance. The event-omission check supports cautious wording about a possible opportunity for March rainfall prediction, rather than a systematic El Niño enhancement.

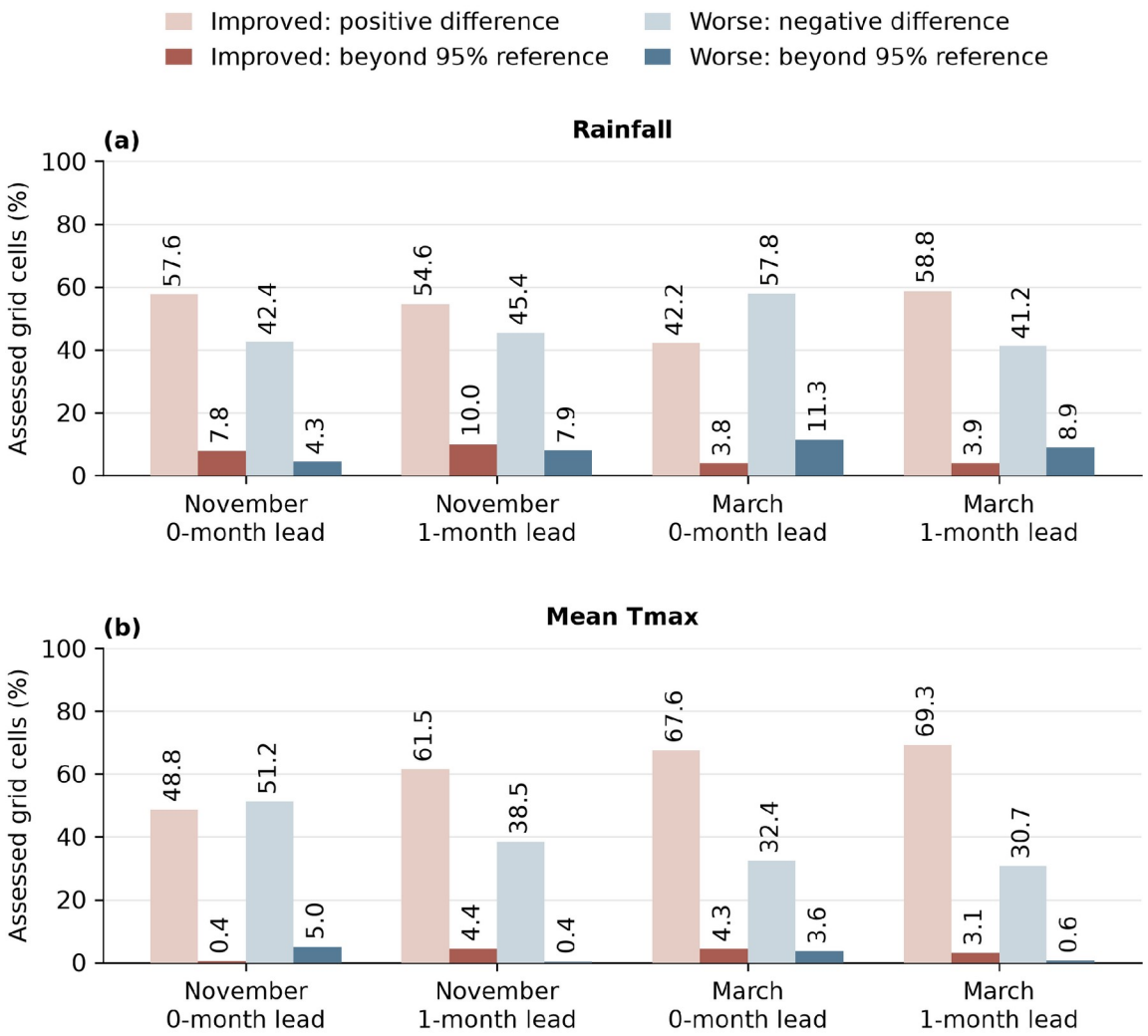


Figure S24. Percentage of assessed grid cells with improved (red) or worse (blue) raw ECMWF anomaly correlation during moderate, strong and very strong El Niño seasons relative to the arithmetic mean of 10,000 equal-sized non-El Niño control subsamples. Panels show cumulative precipitation and mean Tmax for 1–30 November and 1–30 March at 0-month and 1-month lead. Light bars classify the sign of El Niño r minus mean control r; dark bars show the subset where El Niño r lies above the 97.5th or below the 2.5th percentile of control correlations. The same assessment masks, period and control draws as Figure 6 are used.

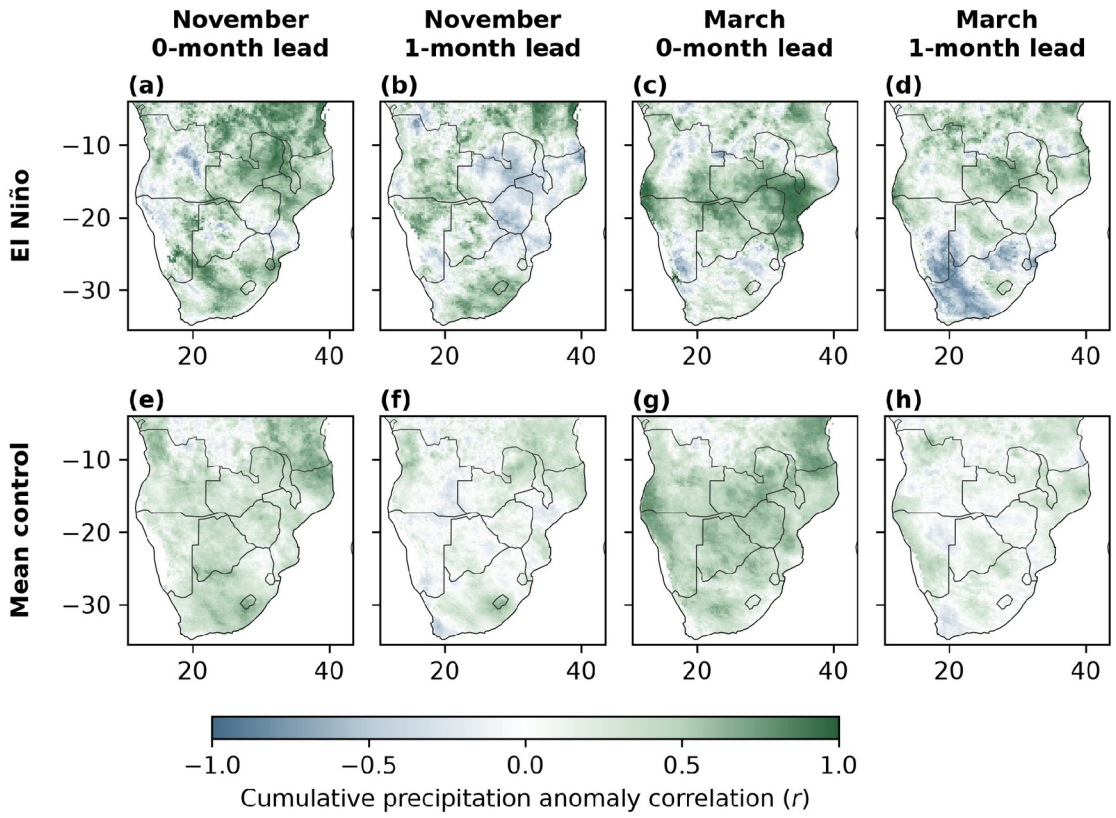


Figure S25. Signed cumulative-precipitation anomaly correlations underlying Figure 6. The upper row is the correlation across selected El Niño seasons; the lower row is the arithmetic mean correlation across 10,000 equally sized control samples. Columns show November and March at 0-month and 1-month lead, using 1 November/1 October and 1 March/1 February initialisations, respectively. Raw ECMWF ensemble-mean cumulative precipitation and mean Tmax are verified against TAMSAT and CPC for 1-30 November and 1–30 March at both leads. Controls are 10,000 random samples of eight or nine years, drawn without replacement from available neutral and La Niña seasons, i.e. excluding all OND ONI ≥0.5°C seasons.

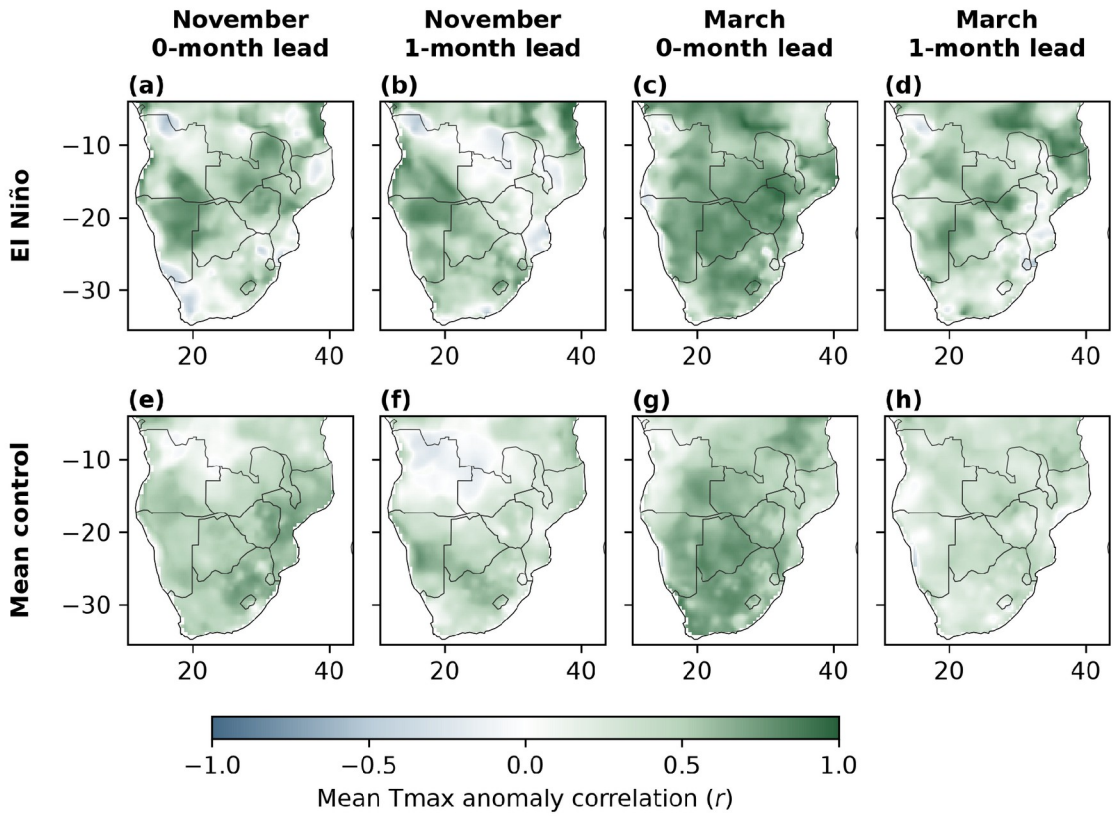


Figure S26. As for Figure S25 but for Tmax.

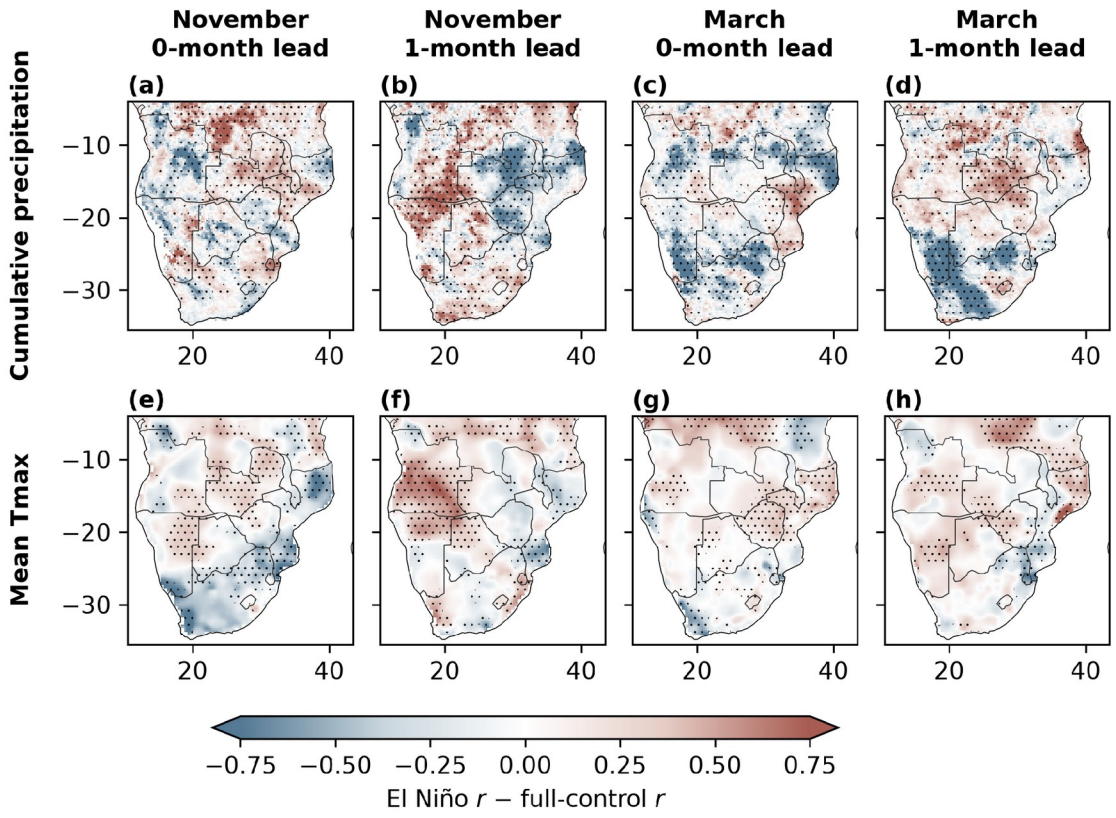


Figure S27. Sensitivity of the ACC comparison to omitting individual El Niño episodes. Colours show full-sample El Niño ACC minus ACC across all available neutral and La Niña control seasons; unlike Figure 6, the control correlation uses the full pool rather than the mean of matched-size samples. Dots mark cells where all omission correlations are defined and the sign is retained after every episode is omitted in turn. Controls remain fixed; 1986/87 and 1987/88 are omitted together. This is an event-influence diagnostic, not a significance test. Rows show cumulative precipitation and mean Tmax; columns show November and March at 0-month and 1-month lead, as in Figure 6. Verification windows are 1–30 November and 1–30 March.

1. Zhang, W., et al., *AHAD: African major crops harvested area dataset for the years of 2000, 2010, and 2020.* Scientific Data, 2025. **12**(1): p. 1691.